The Cryosphere, 19, 4715–4740, 2025 https://doi.org/10.5194/tc-19-4715-2025 © Author(s) 2025. This work is distributed under the Creative Commons Attribution 4.0 License.





High-frequency broadband active acoustic systems as a tool for high-latitude glacial fjord research

Elizabeth Weidner¹, Grant Deane², Arnaud Le Boyer², Matthew H. Alford², Hari Vishnu³, Mandar Chitre^{3,4}, M. Dale Stokes², Oskar Glowacki⁵, Hayden Johnson², and Fiammetta Straneo^{6,7}

Correspondence: Elizabeth Weidner (e.weidner@uconn.edu)

Received: 28 September 2024 – Discussion started: 6 November 2024

Revised: 8 July 2025 - Accepted: 14 August 2025 - Published: 21 October 2025

Abstract. High-frequency broadband scientific echosounders enable the monitoring of complex dynamics, via the rapid collection of high-resolution, near-synoptic observations of the water column and quantitative geophysical measurements. Here, we demonstrate the applicability and utility of broadband active acoustics systems to improve observational capabilities in high-latitude glaciated fjords. These isolated and challenging field locations are a critical environment, linking the terminal end of terrestrial ice fields to the broader ocean, undergoing complex changes due to accelerated high-latitude warming trends. Using broadband (160-240 kHz) acoustic data, collected in tandem with ground-truth measurements from a conductivitytemperature-depth (CTD) and microstructure probe, in Hornsund Fjord in southwest Svalbard, we address the following three topics: (1) variability in the thermohaline structure and mixing across different temporal and spatial scales, (2) identification and characterization of processes in play at dangerous glacier termini, and (3) remote estimation of dissipation rates associated with mixing. Through these analyses, we illustrate the potential of broadband echosounders as a reasonably priced, relatively straightforward addition to experimental field kits, well suited for field deployment in high-latitude fjords where observations are limited by the length of season and generally challenging conditions.

1 Introduction

The ice—water interface of marine-terminating (tidewater) glaciers in high-latitude fjords represents a critical transition zone, linking the terrestrial, cryosphere, and ocean systems. As such, tidewater glaciers are central to not only polar but also global ocean dynamics: contributing to sea level rise through ablation (Joughin et al., 2012, 2004; Nick et al., 2009), modifying ocean properties through freshwater flux (Fichefet et al., 2003; Straneo et al., 2011), altering thermohaline circulation patterns (Bamber et al., 2012; Beaird et al., 2023; Böning et al., 2016; Slater et al., 2018; Straneo and Cenedese, 2015), and supporting highly productive and unique marine ecosystems (Hopwood et al., 2020, 2018; Lydersen et al., 2014). Simultaneously, their direct connection to atmospheric and oceanic forcing, combined with accelerated high-latitude warming trends (England et al., 2021; Holland et al., 2008; Howat et al., 2007; Serreze and Francis, 2006), has resulted in a dramatic increase in glacial retreat rates and ice mass loss over the past 2 decades (Enderlin and Hamilton, 2014; Geyman et al., 2022; van den Broeke et al., 2016). Despite their importance to polar oceanography, many questions remain with respect to quantifying the impact of changing climate on tidewater glacier systems and predicting the subsequent impact of these changes on the broader polar system (e.g., Straneo and Heimbach, 2013).

¹Department of Marine Sciences, University of Connecticut, Groton, MA 06340, USA

²Scripps Institution of Oceanography, University of California San Diego, San Diego, CA 92037, USA

³Acoustic Research Laboratory, National University of Singapore, Singapore, 119227, Singapore

⁴Department of Electrical and Computer Engineering, National University of Singapore, Singapore, 119007, Singapore

⁵Institute of Geophysics, Polish Academy of Sciences, 01-452 Warsaw, Poland

⁶School of Engineering and Applied Sciences, Harvard University, Cambridge, MA 02138, USA

⁷Department of Earth and Planetary Sciences, Harvard University, Cambridge, MA 02138, USA

A central challenge in characterizing these regions lies in the gap between the observational requirements, both in terms of sampling rate and spatial scale, and current capabilities. High-latitude fjords are isolated, often dangerous environments where the research season is short, the presence of ice and poor weather limits direct observation, and the field conditions can be physically and psychologically demanding (Leon et al., 2011; Palinkas and Suedfeld, 2008). Moreover, while traditional in situ measurement techniques, such as conductivity-temperature-depth (CTD) or microstructure profilers, can provide high-resolution vertical profiles of geophysical measurements (e.g., temperature and salinity), they lack spatial context and practical deployment mechanisms in many regions of high-latitude fjords (e.g., near the ice face). Satellite-based data are commonly used for broadscale geophysical observations (Konik et al., 2021; Serreze and Stroeve, 2015); however, the spatial resolution of these data can be coarse (> 10 m; e.g., Sentinel-2 and Landsat-9), depending on the data source. Observations are also often limited by ice and cloud cover and can only provide direct information on the upper meters of the water column (Swift, 1980). These compounded observational challenges often result in qualitative, rather than quantitative, descriptions of critical innerconnected fjord processes, such as the connection between stratification and glacial ablation processes (submarine melting, surface melting, and calving). Enhanced observational capabilities, for both synoptic and in situ quantitative geophysical measurements, are needed to fill the observational gaps in high-latitude fjords and quantify the ongoing impact of the changing climate. The aim of this work is to outline the potential of broadband scientific echosounders to help address questions regarding geophysical processes in glacier terminus environments and other high-latitude coastal regions.

Active acoustic systems can provide the necessary measurements to improve geophysical observational capabilities in high-latitude glaciated fjords. They offer near-synoptic observations of water column dynamics along kilometer-scale tracks on length scales of shorter than 1 m. Acoustic profiles can be collected rapidly, typically at a rate of 0.1-10 Hz, providing coverage of spatial scales from the submeter scale to full-fjord (kilometer) scale and temporal scales ranging from seconds to seasons (Godø et al., 2014; Proni and Apel, 1975). Oceanographic processes have a long history of acoustic observation, such as internal waves (Moum et al., 2003; Orr et al., 2000), hydraulic transitions (Cummins et al., 2006; Farmer and Dungan Smith, 1980), stratification (Holbrook et al., 2003; Penrose and Beer, 1981; Ross and Lavery, 2009; Stranne et al., 2017; Weidner et al., 2020), fish and zooplankton communities (Cotter et al., 2021; Lavery et al., 2010), gas bubbles (Marston et al., 2023; Medwin, 1977; Vagle et al., 2005), suspended sediment (Thorne and Hanes, 2002; Thorne and Hardcastle, 1997; Thorne and Hurther, 2014; Young et al., 1982), and fluid emissions (Bemis et al., 2012; Xu et al., 2017). Active acoustic systems have provided high-resolution bathymetry of polar seas (Björk et al., 2018; Jakobsson et al., 2020), information on fjord circulation patterns (Abib et al., 2024; Sutherland and Straneo, 2012), and information on sea ice extent (Bourke and Garrett, 1987; McLaren et al., 1994; Rothrock and Wensnahan, 2007); however, they remain underused in the study of the coastal water column, although a number of studies have taken place at lower latitudes (e.g., Bassett et al., 2023; Kilcher and Nash, 2010; Lavery et al., 2013). In this article, we discuss the potential of filling current observational gaps in high-latitude glacial fjord systems using high-frequency (> 100 kHz), broadband, scientific split-beam echosounders.

1.1 Overview of scientific echosounders

Scientific echosounders were initially developed as narrowband (single-frequency) tools for fisheries applications (e.g., Jech and Michaels, 2006; Simmonds and MacLennan, 2008) and have a long history of producing qualitative plots of acoustic scattering intensity in the water column across both range and depth (echograms); see Fig. 7 in Farmer and Armi (1999), Fig. 1 in Moum et al. (2003), and Fig. 3 in Jech and Michaels (2006). Changes in acoustic scattering intensity, often represented in echograms by a gradated color scale, are driven by changes in acoustic impedance, a combination of medium density and compressibility (e.g., sound speed). Ocean boundaries, such as the seafloor and surface, and water column phenomena, such as biology, ocean structure, and mixing, are common drivers of acoustic impedance changes. Echogram images provide intuitive and compelling qualitative visualization of oceanic processes and boundaries for applications ranging from target identification in recreational fish finders to long-term environmental monitoring by government agencies (e.g., Jech, 2021) to descriptions of hydrological forcing in highly dynamic environments (e.g., Farmer and Armi, 1999). The echosounder used in this work is a split-beam system, where the receive array is split into quadrants to determine the angle of the arriving signal through split-aperture processing methods (see Burdic, 1991). Measurements of absolute acoustic scattering strength from splitbeam echosounders can be converted into quantitative data streams of important geophysical signals through acousticinversion methods with the proper field calibration procedure (Demer et al., 2015), in situ sampling, and theoretical acoustic scattering models. Given the potential for rapid, remote measurements of geophysical properties of the ocean interior, there has been significant effort directed towards developing inversion methods, including the analysis of turbulent mixing (Goodman, 1990; Moum et al., 2003; Ross and Lueck, 2005; Seim et al., 1995), seafloor sediment characteristics (Amiri-Simkooei et al., 2011; Fonseca and Mayer, 2007; LeBlanc et al., 1992; McGee, 1990), biomass estimates for fisheries management and community analysis (Martin et al., 1996; Sawada et al., 1993), bubble size distributions (Li et al., 2020), and heat flux from hydrothermal plumes (Xu et al., 2017).

The incorporation of broadband capabilities (signal pulses with an extended and continuous frequency range) has dramatically increased the utility of scientific echosounder systems for the quantitative study of oceanic processes. Compared to narrowband systems, broadband echosounders provide increased along-beam (range) resolution - on the order of decimeters to millimeters – and continuous frequency resolution for spectral characterization (Chu and Stanton, 1998; Ehrenberg and Torkelson, 2000). Increased resolution is leveraged by researchers to discriminate closely spaced targets in the water column, facilitating precise positioning and tracking of targets (e.g., Loranger and Weber, 2020; Weidner et al., 2019; Jerram et al., 2015); moreover, continuous frequency-modulated scattering over the pulse bandwidth reduces the ambiguities in the interpretation of the acoustic returns so that specific scattering phenomena can be differentiated and more accurately classified in regions where scattering intensity and spatial context alone are not sufficient (e.g., Lavery et al., 2010; Stanton et al., 2010). Spectral analysis has been leveraged for acoustic-inversion procedures to quantify biomass and determine the community makeup of both plankton (Lavery et al., 2010) and fish (Cotter et al., 2021; Loranger et al., 2022) as well as to differentiate between multiple scattering mechanisms, for example oil droplets and gas bubbles (Loranger and Weber, 2020). A growing body of literature discusses acoustic-inversion methods using commercial broadband echosounders to quantify oceanic phenomena including thermohaline structure (Loranger et al., 2022; Weidner and Weber, 2024), turbulent mixing (Lavery et al., 2013; Muchowski et al., 2022), and gas seeps (Weidner et al., 2019).

1.2 Basics of acoustic data interpretation

In the underwater acoustic community, experience and familiarity with acoustic data interpretation methods is assumed, and therefore embedded in the literature. However, the aim of this paper is to expand the use of broadband acoustic tools in coastal polar regions by engaging a broader audience; thus, here, we cover these topics in some detail.

High-resolution, near-synoptic images collected by active acoustic systems are commonly referred to as echograms. Echograms consist of a series of individual time series records of acoustic scattering intensity, typically collected at uniform time intervals. In the case of split-beam echosounders, individual acoustic profiles are measurements of backscattering intensity due to the monostatic geometry of the co-located transmit and receive array (i.e., the transducer; see Medwin and Clay, 1997, their Sect. 10.1). When a transducer is mounted on a vessel and data are collected while underway, as in this work, the sequential stacking of closely spaced acoustic profiles effectively provides an "image" of the water column in space and time. In this paper,

we refer to data collected in this manner as "near-synoptic observations". We use the term near-synoptic because the time interval between individual acoustic records results in an along-track dimension that is always convolved with time, rather than a truly synoptic "snapshot" of the ocean. As a result, observations of nonstationary phenomena (e.g., internal waves and fish schools) can be aliased, and this effect should be considered in analysis. Regardless of this complexity, echograms provide highly resolved images of the water column that allow for the contextualization and interpretation of oceanic phenomena with resolutions unmatched by other observational means.

There are two types of resolution in an echogram: the along-ray path resolution and along-track resolution. The along-ray path, or range, resolution of an individual acoustic profile is defined by the distance between independent estimates of the backscatter strength. With the application of pulse compression processing techniques, the range resolution of broadband systems is proportional to the inverse of the pulse transducer signal's bandwidth (Chu and Stanton, 1998; Turin, 1960) and typically ranges from millimeter to decimeter scales. The spatial resolution, defined by the distance between individual acoustic profiles in the along-track direction of vessel motion, is a function of the transducer's pulse repetition fire rate (typically 0.1–10 Hz) and duty cycle, the depth of the seafloor, and the speed of the vessel. In nearshore environments, when seafloor depths are relatively shallow (< 150 m), typical spacing between profiles ranges from the sub-meter to the meter scale.

Echograms offer more than just highly resolved images; they contain quantitative information on ocean water column processes and boundaries. Acoustic energy from the outgoing broadband pulse is scattered and reflected from phenomena in both the water column and at boundaries (e.g., seafloor, sea surface, and ice face) that create changes in medium density and sound speed, referred to in the acoustic literature as "impedance contrasts". In the context of the ocean, impedance contrasts are often the result of physical boundaries (see Fig. 2 in Weidner et al., 2020), suspended particulates (plankton, fish, and sediment; see Fig. 2 in Cotter et al., 2021, or Fig. 2 in Loranger et al., 2022), changes in thermohaline-structure-associated pycnoclines (see Fig. 2 in Stranne et al., 2017), and flow or mixing structures (see Fig. 1 in Lavery et al., 2013) within the interior of the water column. Acoustic scattering intensity is often reported on a logarithmic scale (decibels) due to the wide range of potential impedance contrasts associated with ocean boundaries and water column processes. For example, the acoustic scattering intensity recorded from seafloor scattering will be several orders of magnitude higher than scattering from thermohaline structure because the impedance contrast between seawater and rock (or sediment) is significantly greater than the impedance contrast brought about by the transition between water masses. The characteristics of the backscattered signal (e.g., intensity and broadband spectral content) are linked to geophysical properties of oceanic phenomenon (e.g., dissipation rate of turbulent kinetic energy (TKE), bubble size, and biological community assemblage), which can be characterized through acoustic data analysis.

1.3 Potential for acoustic measurements in high-latitude studies

Broadband scientific echosounders represent a powerful tool for coastal studies; however, until recently, the use of broadband analysis methods has been limited in their applicability due to the high cost of custom-made broadband systems, often exceeding USD 500 000. The availability of lower-cost, commercial broadband systems and the expanded access to a broader user base has resulted in a growing body of literature and processing software for broadband data analysis (Blomberg et al., 2018; Cotter et al., 2019; Demer et al., 2017; Lavery et al., 2017; Weidner et al., 2019). Hence, these systems have the potential to improve observational capabilities in isolated and challenging field locations. This paper will address the acoustic analysis of three topics within the study of high-latitude systems:

- 1. variability in the thermohaline structure and mixing across different temporal and spatial scales,
- 2. identification and characterization of processes in play at dangerous glacier termini, and
- 3. remote geophysical parameter estimation.

Characterizing the distribution of water masses in highlatitude fjords is complicated by the presence of ocean and glacially derived water masses (e.g., submarine melting and subglacial discharge) and by fjord-scale processes with intense spatial and temporal variability (Hager et al., 2022; Straneo et al., 2011). Elevated levels of vertical mixing in fjords are driven by strong, intermittent turbulence associated with the tidal cycle and steep bathymetric features, such as terminal moraines (Farmer and Armi, 1999; Schaffer et al., 2020; Smyth and Moum, 2001). Additionally, the degree of stratification (Geyer and Ralston, 2011), local meteorological conditions (Slater et al., 2018; Straneo and Cenedese, 2015), and sill-driven reflux (Hager et al., 2022) can influence circulation dynamics and, therefore, thermohaline structure.

Traditionally, water masses are characterized through the in situ collection of CTD profiles. Thermohaline structure can be inferred by interpolating between CTD profiles – the denser the profile collection, the more accurate the measurements of the spatial distribution of thermohaline structure. Despite their ubiquity and utility, disentangling interconnected processes controlling thermohaline structure can be challenging using direct observational measurements alone. Individual profiles lack spatial context, and dense profile collection can be cost- and time-prohibitive. Acoustic observations can be leveraged to assist in mapping out and characterizing water column structure through imaging of the bound-

aries (pycnoclines) between water masses. Scattering at water mass boundaries (e.g., pycnoclines) is well documented in the literature and connected to a number of scattering mechanisms, including the sharp gradients in thermohaline structure (e.g., Stranne et al., 2017; Weidner et al., 2020), the intense turbulent mixing due to shear forces (Geyer et al., 2017; Lavery et al., 2013), and the suspended particles (such as biological aggregations, e.g., Benoit-Bird et al., 2009, or sediment, e.g., Simmons et al., 2020) that are often associated with thermohaline structure. The inclusion of broadband acoustic data along with direct sampling can elucidate the fjord-scale dynamics that control the distribution of thermohaline structure.

Beyond the near-synoptic observations, echosounders can collect measurements in regions inaccessible to direct sampling equipment. In high-latitude glacial fjords, this remote advantage can be leveraged to collect measurements in dangerous regions, such as a submerged ice-ocean interface of the glacial terminus. Direct observations at the ice edge are sparse in the literature, owing to limited access due to the presence of ice mélange and icebergs. Furthermore, calving events, both subaerial and submarine, make work at the ice face dangerous for vessels, equipment, and personnel, thereby precluding most ship-based sampling. Oceanographic data, such as CTD casts, are generally collected downstream in the fjord, and ice-ocean dynamics are then inferred (Beaird et al., 2023; Stevens et al., 2016; Straneo et al., 2011). The few existing in situ observations have been collected by helicopters (Bendtsen et al., 2015), remotely operated vehicles (Mankoff et al., 2016), and sensors attached to marine mammals (Everett et al., 2018). The paucity of direct measurements limits the inclusion of terminus iceocean dynamics in large-scale climate models (Bamber et al., 2018), predictions of fjord circulation (Straneo et al., 2011), and contribution to sea level rise predictions (Siegert et al., 2020). The need for enhanced observational capabilities and additional measurements at the ice-ocean interface has been well documented (e.g., by Siegert et al., 2020).

A number of recent studies have employed acoustic systems to overcome the challenges associated with nearterminus observations. Sutherland et al. (2019) estimated submarine melt rates by combining high-resolution images of the submerged terminus from a multibeam echosounder with data on glacier motion. An acoustic Doppler current profiler (ADCP), deployed from an autonomous surface vehicle by Jackson et al. (2020), provided the first characterization of meltwater intrusions in the near-terminus region. Broadband echosounders can add to this acoustic toolset by providing remote, quantitative observations of the iceocean interface and those processes occurring nearby, such as subglacial discharge. Uniquely, broadband echosounders can make measurements of absolute scattering intensity, which is not possible with other acoustic systems, and these measurements, combined with split-aperture processing and broadband spectral analysis, can shed light on the morphology of the terminus, identify the presence and constrain the geometry of subglacial discharge plumes, and identify innerconnection biophysical processes occurring near the terminus.

Finally, quantitative analysis of broadband spectral data can be used to identify scattering mechanisms and even provide remote measurements of geophysical signals (e.g., dissipation rates of TKE and gas bubble size). These methods compare the calibrated, absolute scattering measurements of a specific phenomenon made by field echosounders to predicted scattering levels from theoretical acoustic scattering models. The models are generally informed by in situ measurements of the physical (e.g., thermohaline structure, bubbles, and suspended sediments) or biological scattering mechanisms, collected in tandem with the acoustic field measurements. The direct comparison of scattering levels allows for inversion for geophysical parameters from rapid, highresolution, near-synoptic, echosounder observations and offers a promising alternative to traditional direct sampling approaches in challenging locations.

The aim of this paper is to demonstrate the applicability and utility of active acoustics systems to high-latitude systems using a high-frequency (160-240 kHz), broadband acoustic dataset collected in Hornsund Fjord, Svalbard. Section 2 of this paper provides an overview of the field site in Svalbard. The equipment, vessel, and data collection methods are described in Sect. 3. Section 4 covers the analysis of high-resolution water column observations in tandem with direct sampling to characterize dynamics across the full-fjord scale, as well as the potential for remote measurements in the dangerous region of the submerged glacial terminus. Section 4 also includes a discussion of broadband spectral analysis and acoustic-inversion efforts to remotely measure turbulent mixing associated with fjord bathymetry and tidal forcing. A discussion of the acoustic data collection methods and analysis, including safety considerations for glacial systems and limitations of broadband systems, is covered in Sect. 5. Section 6 concludes the paper with the potential for future applications of broadband systems to high-latitude fjords.

2 Study site

Hornsund Fjord is a highly glaciated, $\sim 35\,\mathrm{km}$ long fjord located in southwest Spitsbergen, Svalbard (Fig. 1). Glaciers cover approximately $67\,\%$ ($802\,\mathrm{km}^2$) of the total area of Hornsund Fjord, with tidewater glaciers constituting $97\,\%$ of its glacierized area (Błaszczyk et al., 2013). The western coast of Svalbard, including Hornsund Fjord, is influenced mainly by the North Atlantic Ocean current (Walczowski and Piechura, 2006). The mean annual air temperature trend of the region over the last 4 decades is more than $+1.14\,^\circ\mathrm{C}$ per decade – a rate 6 times higher than the global average (Wawrzyniak and Osuch, 2020). Tidewater glaciers in Hornsund Fjord are retreating at an average rate of ~ 70 –

100 m yr⁻¹ (Błaszczyk et al., 2023, 2013), which is among the highest rates in Svalbard.

Data collection in Hornsund took place in the glaciated bay of Hansbukta and at the calving front of the retreating, grounded tidewater glacier Hansbreen. The bathymetry of Hansbukta is dominated by rapid shallowing from a main channel of Hornsund Fjord ($\sim 200 \,\mathrm{m}$ deep) to a well-defined transverse ridge (3-15 m deep), which is interpreted as the terminal moraine of Hansbreen (Ćwiakała et al., 2018). A series of smaller transverse ridges, plow marks, depression areas, and pockmarks characterize the bathymetry of inner Hansbukta approaching the terminus of Hansbreen. Hansbreen is a polythermal glacier with a mixed basal thermal regime and covers an area of $\sim 54 \, \mathrm{km}^2$ (Błaszczyk et al., 2013). The calving front of Hansbreen is 1.7 km long (Błaszczyk et al., 2019), grounding at ~ 70 m depth, and has retreated on average 38 m yr⁻¹ between 1992 and 2015 (with a maximum rate of $311 \,\mathrm{m\,yr^{-1}}$), which is more than twice its historical rate (Błaszczyk et al., 2021; Grabiec et al., 2018). Svalbard's enhanced warming trends combined with Hansbreen's long history of study (e.g., Kosiba, 1960) and close proximity to the Polish Polar Station Hornsund makes this an excellent field site for acoustic data collection and methods.

3 Data collection methods

Data were collected between 6 and 12 July 2023 aboard the marine vessel (MV) Ulla Rinman and included broadband acoustic backscattering data throughout the water column, conductivity-temperature-depth (CTD) profiles, microstructure casts, and time-lapse imagery (Fig. 2). Acoustic data were collected with a Simrad EK80 wideband transceiver transmitting with a Simrad ES200-7CD split-beam transducer with a 7° circular beam and frequency range of 160-240 kHz. The transducer was deployed from a 6 m long sidemount pole with two geometries during the field campaign: downward- and side-looking. The transducer was mounted directly to the vertical pole for the downward-looking geometry. For the side-looking geometry, a 3D-printed plate adaptor provided a 10° declination angle relative to the horizontal. The system was operated continuously during survey operations, and all acoustic system parameters (i.e., transmit power, signal mode, pulse length, and frequency range) were kept constant during acquisition. The acoustic system was calibrated using a 25.0 mm tungsten-carbide sphere during field operations on 6 July 2023 and in the Chase engineering tank at the University of New Hampshire with 25.0 and 38.1 mm tungsten-carbide spheres on 13 March 2024, following the procedure described in Demer et al. (2015).

Position and attitude data were collected and applied to the field data in post-processing from an SBG system Ellipse-D inertial navigation system (INS). The INS was mobilized on the bridge, and the antennas were mobilized on the bridge deck railing of MV *Ulla Rinman*, with a clear sky view and

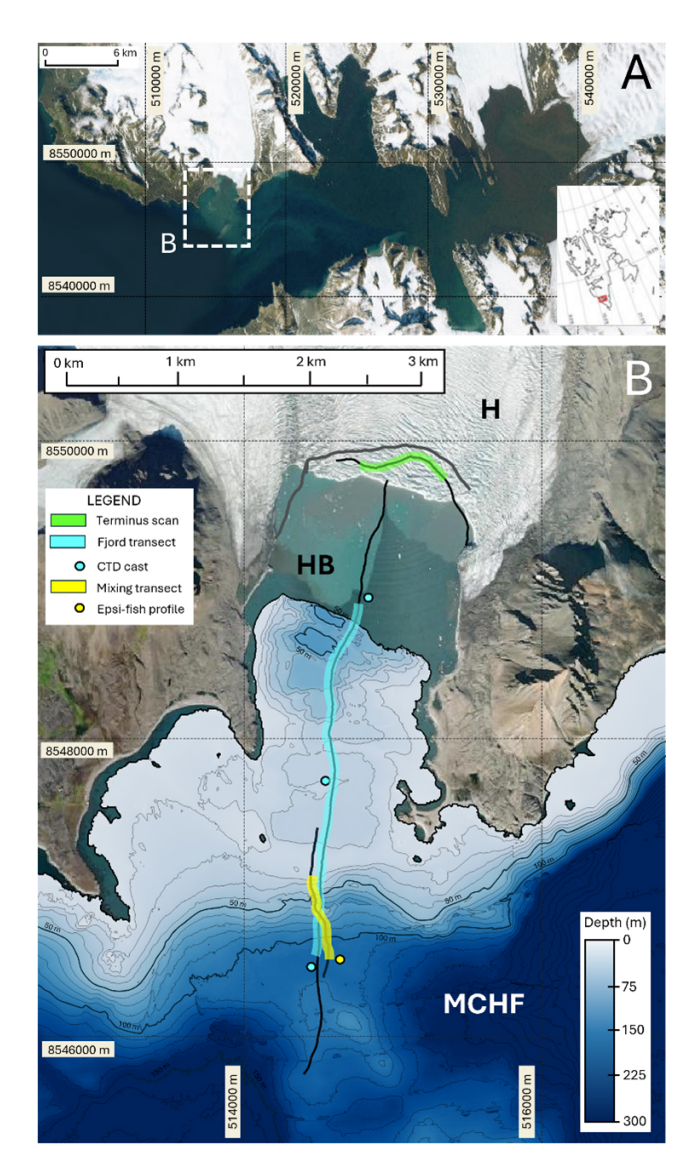


Figure 1. The general location of the 2023 field program in Hornsund Fjord, Spitsbergen, Svalbard (A). The region of study in Hornsund Fjord is identified by the inset box (B) in panel (A) and is illustrated in panel (B). The background image is from Landsat-8 imagery collected in June 2023, courtesy of the US Geological Survey, Department of the Interior. Multibeam bathymetry of Hornsund Fjord (MCHF) and Hansbukta (HB) is provided by Błaszczyk et al. (2021) and the Norwegian Hydrographic Service. Bathymetric coverage of Hansbukta does not fully cover the region of study due to the retreat of Hansbreen (H) since the most recent seafloor survey. The position of Hansbreen's terminus during operations in July 2023 was estimated using MV Ulla Rinman's radar and is denoted by the gray line. The black lines running north-south across Hansbukta and parallel to Hansbreen are the tracks of MV Ulla Rinman during broadband acoustic data collection. Highlighted regions identify the extent of echograms from Fig. 3 (blue), Fig. 4 (green), and Fig. 5 (yellow). Circular markers are the positions of the CTD casts (Fig. 3) and Epsi-fish profile (Fig. 5).

more than 2 m of separation. The INS provided horizontal and vertical positioning accuracies of 1.2 and 1.5 m, respectively. Pitch and roll accuracies were 0.1° and heading accuracy was 0.2° for 1 m baseline.

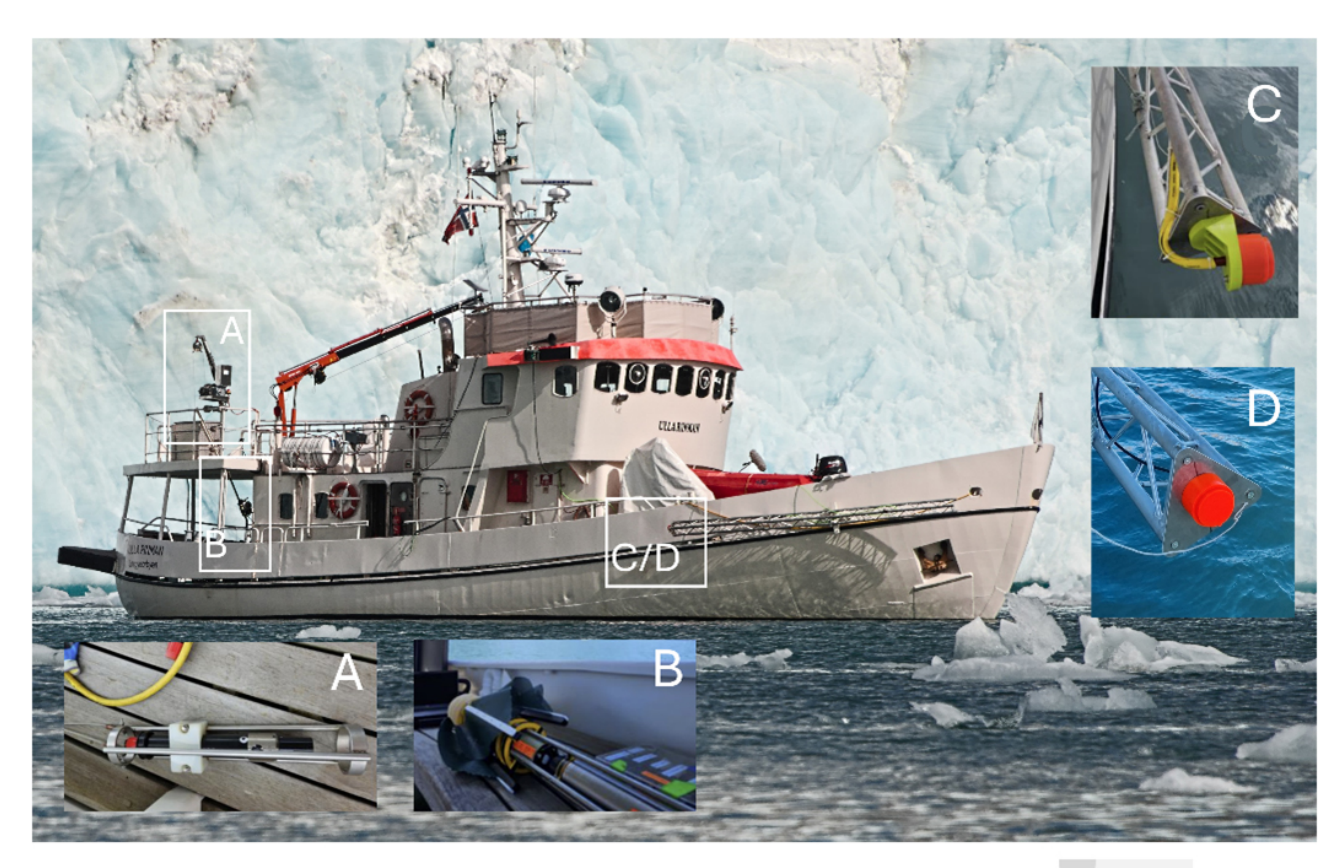
Ground-truth data were collected by two in situ sensors, a Valeport miniCTD sensor and an Epsilometer microstructure probe, "Epsi-fish" (Le Boyer et al., 2021). The Valeport miniCTD unit provided vertical profiles of water column temperature and salinity and was deployed via MV Ulla Rinman's winch. The accuracies of the pressure, conductivity, and temperature measurements from the Valeport miniCTD unit were $\pm 0.05\%$ of full range (300 m), ± 0.01 mS m⁻¹, and ±0.01 °C, respectively. The Epsi-fish, deployed from a commercial fishing reel, provided a total of seven profiles of thermal (χ_T) and turbulent kinetic energy (ε) dissipation rates. The Epsi-fish was developed at Scripps Institution of Oceanography by the Multiscale Ocean Dynamics group. A full description of the Epsi-fish sensors, accuracies, and deployment considerations can be found in Le Boyer et al. (2021). Additionally, two GoPro HERO11 time-lapse cameras were deployed to capture images of ice coverage (ice mélange and icebergs) and other surface expressions in the fjord during survey operations. A complete description of the field deployment, data collection procedure, and data processing details can be found in Appendix A and B.

4 Interpretation and analysis of broadband echosounder data

Broadband echosounder data collected in Hornsund Fjord are used here to demonstrate methods for backscatter data interpretation and analysis in the following sections: the contextualization and characterization of fjord-scale thermohaline structure using acoustic observations and direct sampling (Sect. 4.1), leveraging the remote nature of acoustic measurements to observe the largely inaccessible submerged terminus (Sect. 4.2), and the quantitative analysis of tidally and bathymetrically forced mixing through broadband acoustic-inversion methods (Sect. 4.3).

4.1 Characterizing thermohaline structure in Hansbukta

Acoustic transects of Hansbukta were collected alongside in situ sampling with the miniCTD sensor. The acoustic transects ran along a north–south heading from the deep channel at the mouth of Hornsund Fjord into Hansbukta to the submerged terminus of Hansbreen (see Fig. 1). The echogram in Fig. 3 illustrates a section of one such transect, approximately 1.7 km long and collected over a period of 35 min during the peak ebb tide. The complex, glacially derived bathymetry of Hansbukta is captured and is the strongest scatterer in the echogram (> $-20\,\mathrm{dB}\,\mathrm{re}\,\mathrm{m}^{-1}$). Running from south to north, the bathymetry transitions from the deep



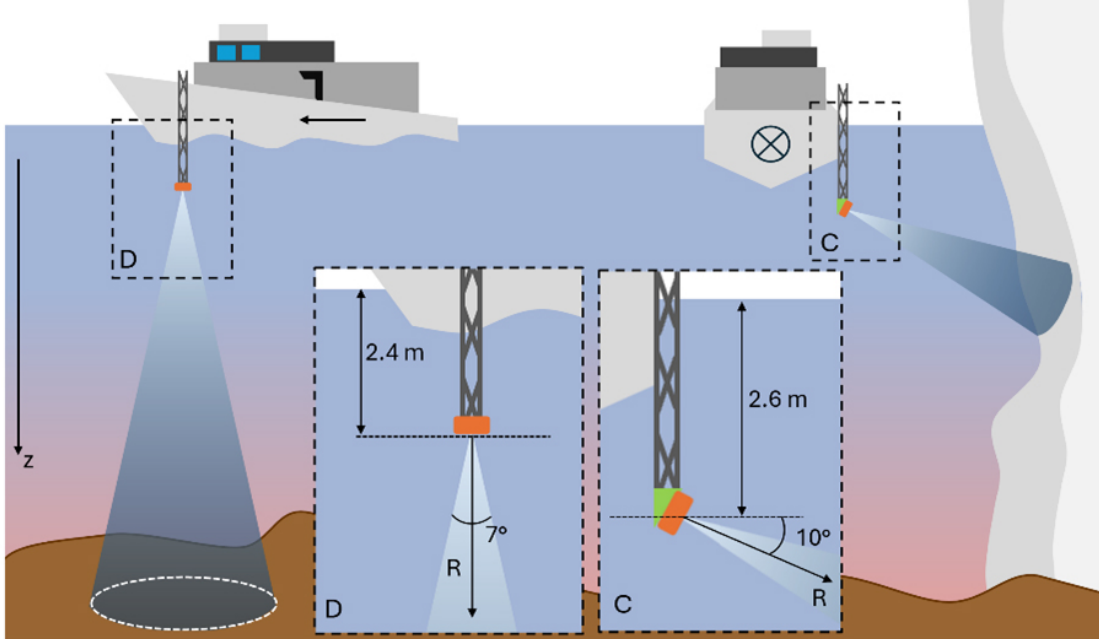


Figure 2. The acoustic survey platform, MV *Ulla Rinman*. The ground-truth systems, CTD and microstructure profiler, were deployed from the starboard aft of the ship. Inset box (**A**) illustrates the deployment setup for the CTD sensor using the ship's winch. Inset box (**B**) illustrates the microstructure probe deployment site from a commercial fishing reel. The broadband acoustic transducer was deployed forward, on the starboard side by a side-mounted pole in two geometries; see inset boxes (**C**) and (**D**) in the top image. The side-looking geometry (box **C**) used a 3D-printed mount plate adaptor to achieve a 10° declination angle from horizontal and was used to collect acoustic scans of the submerged ice face of Hansbreen. The downward-looking geometry (box **D**) was used to collect fjord-scale transects.

(> 200 m) main channel of Hornsund Fjord to the glacial trough of Hansbreen, where the grounding line is approximately 65 m deep. Between the main channel and Hansbreen, the seafloor shallows rapidly over a series of sills, transitioning rapidly from > 200 to 12 m in depth over less than 250 m along the track. In the water column, numerous scattering phenomenon are represented. Biological scattering from individual fish and aggregations are observable, primarily in the main channel (1400–1700 m along the track) and glacial trough (0-200 m along the track), as discrete and small features or larger semicircular regions of elevated scattering between -25 and -35 dB re m⁻¹. Scattering associated with the evolving thermohaline structure across Hansbukta is also observable as weakly scattering $(< -50 \,\mathrm{dB}\,\mathrm{re}\,\mathrm{m}^{-1})$ semidiscrete layers in the upper 20 m of the water column. Several layer-like features evolve over the length of the transect and are discussed below using the CTD data for context. Three miniCTD profiles were collected at key locations along the transect: in the main channel, at the shallowest point of the primary sill, and in the inner fjord. The CTD profiles provide direct measurements of the thermohaline structure at discrete locations across Hansbukta, while the broadband echogram provides spatial context on water mass evolution and the hydrodynamic processes influencing thermohaline structure.

Generally, the thermohaline structure in Hansbukta can be influenced by two external water masses: Atlantic Water (AW) transported on the West Spitsbergen Current, characterized as both warm and saline (3.5 to 6.0 °C, > 35 PSU) (Strzelewicz et al., 2022; Walczowski, 2013), and the relatively cold and saline waters (-1.5 to 1.5 °C, 34.3 to 34.8 PSU) originating from western Svalbard carried on the Sørkapp Current (SC) (Cottier et al., 2005; Promińska et al., 2018). Additionally, submarine glacial discharge and submarine meltwater from ablation, melting, and runoff associated with Hansbreen are introduced into the glacial trough of Hansbukta. Discharge rates from Hansbreen are variable depending on the season, primarily peaking between June and September (Błaszczyk et al., 2019).

The three CTD casts can fingerprint the external and glacially influenced water masses and provide a coarse view of the distribution of thermohaline structure across Hansbukta. At the southernmost extent of the transect in the main channel of Hornsund Fjord (> 20 m), the CTD profile shows that the deep water column can be described as Transformed Atlantic Water (TAW; Fig. 3), the product of entrainments and mixing between AW and SC waters (Nilsen et al., 2008); however, the cold and saline TAW waters are isolated by the shallow sill of Hansbukta and are absent in the sill and glacial trough CTD profiles. At the surface, all of the CTD profiles show a well-mixed surface layer (SL; Fig. 3), characterized by relatively warm and fresh water, likely influenced by submarine glacial discharge and submarine meltwater from Hansbreen. The vertical extent of SL water deepens and warms between the glacial trough and the sills, from 2.0 to 7.5 m in depth and from 3.6 to 4.7 °C, and then retains the same depth and T-S characteristics between the sill and main channel. Below the surface layer, the thermohaline structure of the water column from the main channel of Hornsund Fjord, over the sills, to the glacial trough shows nearly identical T-S characteristics, influenced by sill mixing (SM; Fig. 3). SM water is defined by increasing salinity and a temperature inversion with increasing depth. SM water has a minimum temperature of 2.7 °C and shallows in depth from 12.2 to 6.5 m between the glacial trough and the sill CTD casts. It extends over the water column of the sills and glacial trough CTD casts from the base of the submarine glacial-discharge-influenced surface layer to the seafloor, while in the main channel, it is bounded by a depth approximately equal to that of the shallowest sill depth $(\sim 12 \,\mathrm{m})$. Overall, the CTD data suggest that the influence of Hansbreen extends across Hansbukta well into the main channel of Hornsund Fjord, as evidenced by the persistent, low-salinity SL water across all casts. Furthermore, there is evidence of strong connectivity between the deeper SM water mass in the glacial trough of Hansbukta and in the main channel of Hornsund Fjord; SM water is characterized by the low-temperature intrusion layer seen in all three T-S plots. SM water is constrained by the sill depth in the main channel, suggesting a bathymetric control on not only the thermohaline structure but also the transport of heat and salt between the main channel of Hornsund and the inner bay of Hansbukta and the ice-ocean interface of Hansbreen. However, without additional casts or other information, disentangling the interconnected processes that are controlling the spatial distribution of SL, SM, and TAW water in Hansbukta and the broader transport of heat and salt across Hornsund Fjord (e.g., tides, bathymetry, and glacial discharge rates) remains out of reach.

The broadband acoustic data collected between the CTD casts offer the potential to more fully characterize the distribution of thermohaline structure across Hansbukta and start to explain the dynamics behind evolution observed in the in situ profiles. The water mass boundaries identified by the CTD casts are clearly visible in the echogram as regions of elevated scattering, as illustrated by the dashed gray lines in Fig. 3. The mechanism in the water column responsible for the elevated scattering signal is not immediately clear from visual inspection of the echogram and could be tied to a number of processes (e.g., gradients in T-S, mixing, and biological or sediment particulates); however, these regions show general agreement in their position (depth) with the in situ data on water mass boundaries. Unlike the in situ data, the echogram allows for precise positioning of the visible boundaries across the entire transect of Hansbukta, and the nature of the scattered signal (e.g., shape and intensity) provides context on the active mixing processes occurring in the water column.

Starting with the surface layer, SL waters can be identified by the scattering associated with the sharp gradient in temperature and salinity that occurs at the boundary between

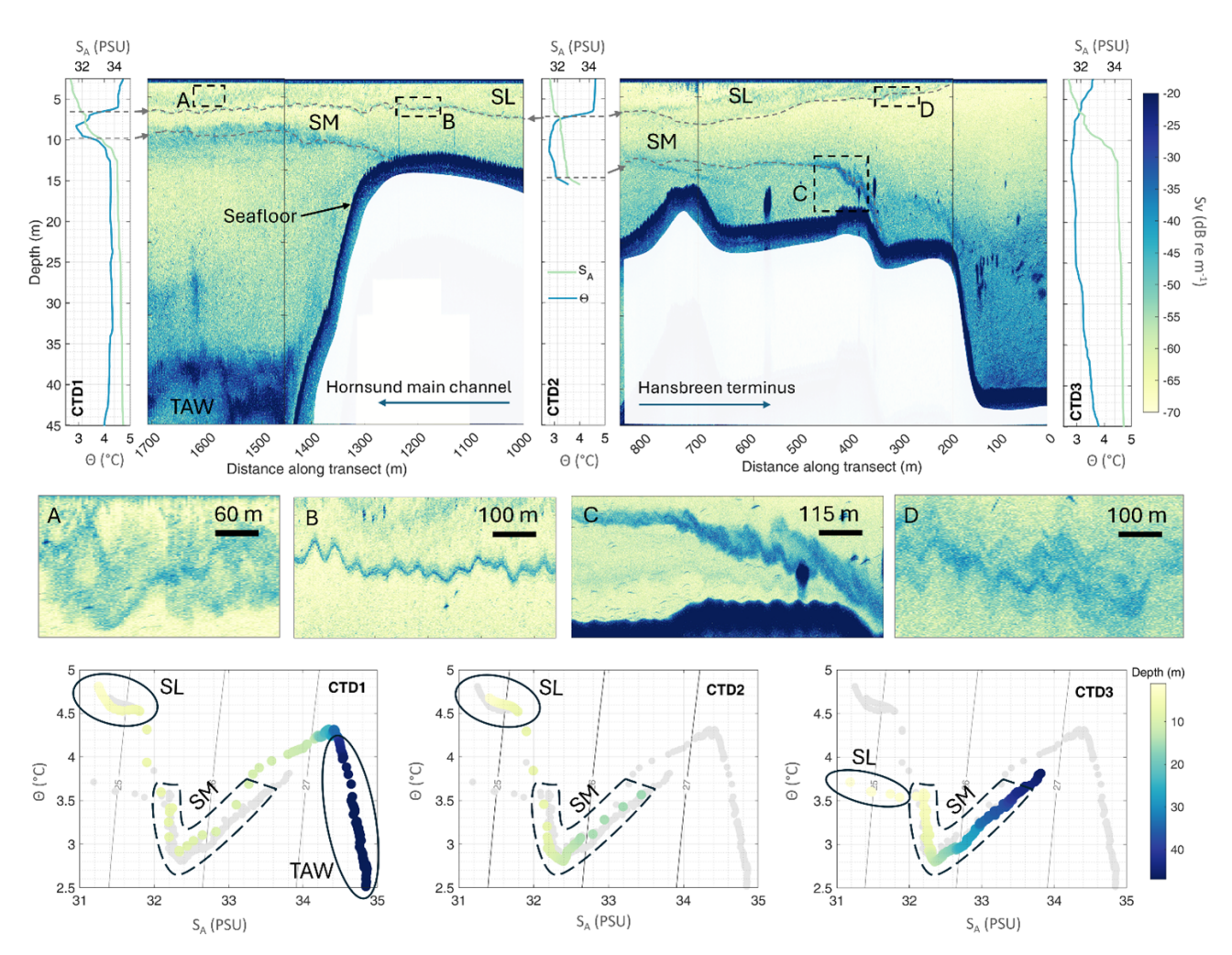


Figure 3. The top panel is an example broadband acoustic transect collected in Hansbukta over the shallow sills separating Hansbreen (right) from the primary channel of Hornsund Fjord (left). See Fig. 1 (highlighted blue transect lines and blue markers) for the transect and CTD cast locations within the larger study site. The echogram is colored using a logarithmic scale by volumetric scattering strength (S_v). Three CTD casts were collected: at the beginning of the transect (CTD 1), at the end of the transect (CTD 3), and at the shallow point of the terminal moraine of Hansbreen (CTD 2). The CTD profiles of conservative temperature (Θ) and absolute salinity (S_A) are plotted against depth in their approximate cast position with reference to the acoustic transect. During CTD cast collection, the acoustic data collection was paused, resulting in the break in the echogram over the sill. The maximum depth of the echogram was limited to 45 m to best illustrate the area of interest in the thermohaline structure. Regions of particular interest are highlighted in boxes (A)–(D), and zoomed-in views are illustrated below the echogram. The bottom set of panels show the temperature–salinity (T–S) diagrams, illustrating the connectivity of waters across Hansbukta and the influence of specific water masses. T–S diagrams plot absolute salinity against conservative temperature for all three CTD casts, colored by depth. On each plot, the T–S data from the other two casts are plotted in light gray for comparative purposes. Specific water masses are noted, including Transformed Atlantic Water (TAW), the region influenced by sill mixing (SM), and the surface layer (SL).

the base of the surface and the intermediate water mass below. While this boundary is not visible in the glacial trough (< 200 m along the track) because the depth of the surface layer is shallower than the draft plus the blanking distance of the transducer, beyond this point the boundary can be tracked as it progressively deepens from the glacial trough over the sills and to the main channel. The nature of the scattering associated with this boundary evolves along the track, elucidating the processes that modify the water mass, as measured in the CTD casts. At the onset of the sills, the boundary is

characterized by a series of Kelvin–Helmholtz (KH) instabilities (Fig. 3, inset box A), recognized by their alternating braid-core structure (e.g., Thorpe, 1987; van Haren and Gostiaux, 2010). KH instabilities are regions of intense shear and turbulent mixing and have been imaged acoustically in other highly energetic coastal regions (Geyer et al., 2017; Lavery et al., 2013). Here, the shear is likely generated by the southflowing current at the surface driven by the ebb tide, potentially combined with the shallowing bathymetry of the sills, evidenced by the presence and directionality of the KH shear

instability structure. The mixing between the surface layer and the intermediate water mass below explains the deepening and change in surface layer properties observed in the CTD casts. Beyond the sills, starting at $1000\,\mathrm{m}$ along the track (Fig. 3), the boundary of the surface layer becomes a discrete, thin scattering layer. The lack of KH instabilities, suggests scattering from a sharp gradient associated with the pycnocline (e.g., Stranne et al., 2017; Weidner et al., 2020), with little mixing or modification in the boundary properties; these observations suggest that the surface layer should have similar T-S properties between the sill and main channel, as was observed in the CTD profiles.

Deeper in the water column there is intense scattering from KH shear instabilities closely associated with the rapid changes in bathymetry at either end of the sills (Fig. 3). In the inner fjord at the onset of each sill, trains of KH instabilities are visible, closely tracking the seafloor depth. The strongest scattering is associated with the second sill, starting at approximately 300 m along the track. Given the close contact with the seafloor, the elevated scattering levels associated with the KH instabilities could be driven by resuspended sediment from strong currents, entrained organisms, or from turbulent microstructure; in either case, the observations from the echogram point to intense mixing in the inner fjord near the seafloor and the transport of water across the sills, likely driven primarily by the changing tide. On the far side of the outermost sill, entering the main channel of Hornsund Fjord, there is a region of elevated scattering centered at approximately 10 m depth that starts at the sill edge and continues for an along-track distance of more than 400 m to the end of the echogram record (Fig. 3). The depth of elevated scattering matches the base of the intermediate water mass identified in the CTD casts by the strong temperature inversion, while the nature of the scattered signal points to an active mixing process, although the braided structure of KH instabilities is not as clear as those in the inner sill area. Again, observations from the echogram point to water mass transport over the sill and explain the connection in T-S properties between the intermediate waters of the main channel of Hornsund Fjord and the inner bay of Hansbukta in the glacial trough.

Overall, the combination of the near-synoptic acoustic observations and the in situ CTD measurements points to a combination of tidally induced flow and shallow sills controlling the intermediate thermohaline structure across Hansbukta, while a surface layer influenced by submarine glacial discharge is persistent throughout Hansbukta. Tidal pumping is identified as the driving process for water mass transport and transformation from (1) the presence and directionality of the KH instabilities that develop at the interface between water masses and the sills, as imaged in the echogram, and (2) the resulting connectivity of the thermohaline structure, measured directly by the CTD casts. This type of stratified flow over topography is well defined in the literature (e.g., Farmer and Armi, 1999; Geyer et al., 2017) and has been ob-

served in estuaries, as well as in terrestrial systems such as mountain ranges (Lilly, 1978). This conclusion is supported by previous research in Hornsund Fjord, which suggests that tidal forcing is the main hydrodynamic driver of heat, salt, and freshwater budgets (Jakacki et al., 2017; Kowalik et al., 2015). The analysis of the transect in Fig. 3 illustrates the utility of broadband echosounder data as a contextual tool for the study of high-latitude systems and the importance of direct sampling sensors, such as CTDs, to inform the analysis and vice versa. The CTD profiles lack the high-resolution spatial context to directly determine the dynamics driving the thermohaline variability, while the acoustic observations are inherently ambiguous, requiring ground-truth information for a complete analysis. Here, a combination of the nearsynoptic acoustic observations with the in situ measurements of the thermohaline structure can provide important physical context for interpretation of the driving oceanographic processes.

4.2 Remote observations of the ice-ocean interface

Measurements of the submerged terminus of Hansbreen were collected using a side-looking geometry (Fig. 2). A series of survey lines were run for approximately 1.2 km parallel to the ice face from east to west, limited by the shallowing seafloor edges of Hansbukta. The transducer geometry provided a diagonal slice of water column observations starting at a depth of 2.6 m (transducer draft) to between 17 and 25 m deep at the submerged terminus (see Appendix B for additional information). The resulting echogram provides imagery of the submerged terminus as well as near-terminus water column phenomena occurring between the transducer and the ice face, including scattering from subglacial discharge (Fig. 4). Concurrently with broadband data collection, water surface imagery was collected with a time-lapse camera. During survey operations near Hansbreen, the surface expression of a subglacial discharge plume was observed as a persistent ice-free region extending outwards from the ice face $< 200 \,\mathrm{m}$. No surface flow velocity measurements were made, but a distinct boundary was observed at the edge of the plume, marked by the ring of ice mélange and a change in surface texture. Observations are consistent with the surfacing of buoyant subglacial discharge reported in the literature (Chauché et al., 2014; Mankoff et al., 2016; Mortensen et al., 2013; Motyka et al., 2003; Xu et al., 2013).

Broadband echosounders can precisely position the submerged terminus, as well as providing measurements of the ice face along-track geometry (Fig. 4). In the echogram, the terminus is easily identifiable across the entire transect by an elongated, strong backscattering return ($>-40\,\mathrm{dB}\,\mathrm{re}\,\mathrm{m}^{-1}$) starting between 75 and 120 m in range. The elongated return from the submerged ice face is initially characterized by the sidelobe return, a weakly scattering signal of a variable length (i.e., between approximately 475–550 and 675–700 m along the track). The primary return from the submerged ter-

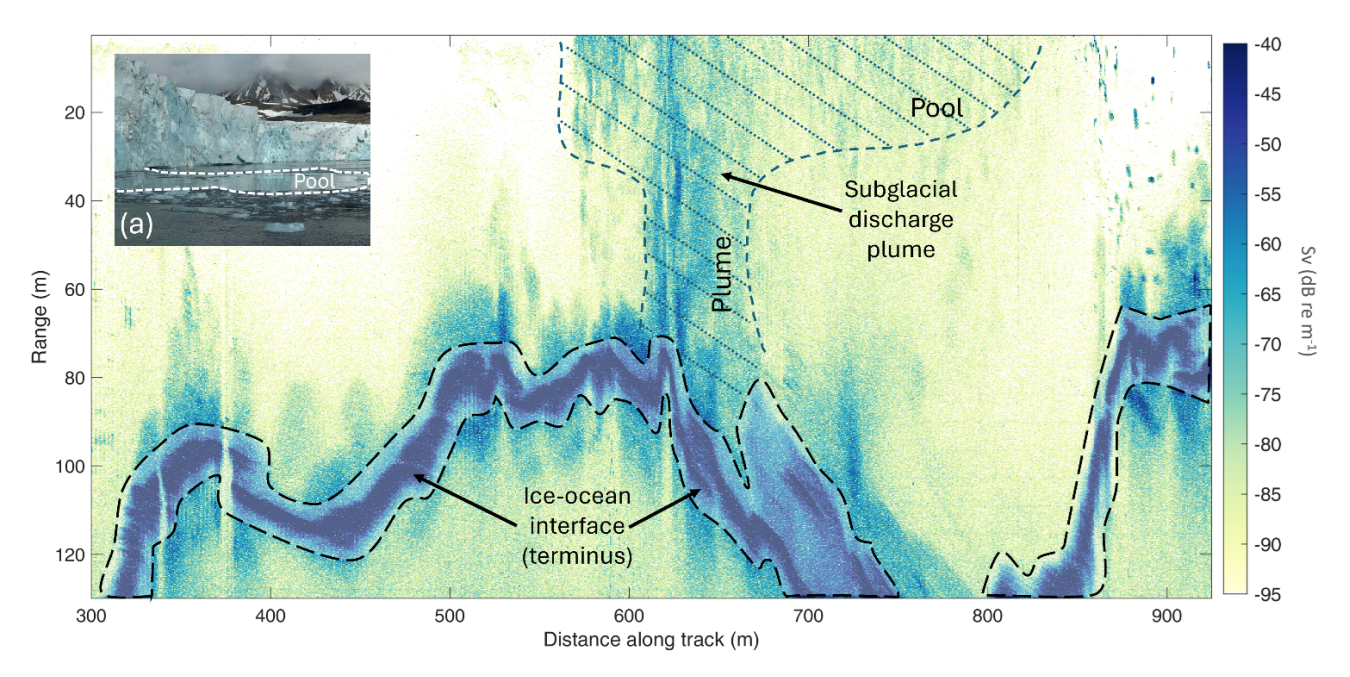


Figure 4. Broadband acoustic observations of the submerged terminus of Hansbreen and the surface expression from the time-lapse imagery (inset box **a**). See Fig. 1 (highlighted green transect lines) for the transect location within the larger study site. The ice—ocean interface of Hansbreen is bounded by the thick dashed black line. The submerged expression of the subglacial discharge plume and its evolution to the surface pool is marked by the dashed dark-blue line; the plume and pool extent were determined from manual interpretation of the elevated scattering intensity in the water column. Potential subglacial discharge, which does not reach the surface, may also be located between 350 and 400 m along the track.

minus shows a generally monotonic increase to a peak intensity value, before a gradual reduction in intensity. The length of the primary return is variable, likely due to variability in the angle of ice face tilt with respect to the transducer. This type of elongated return resulting from oblique incidence geometry and the propagation of the acoustic pulse along an extended surface target has been observed in other broadband echosounder work (e.g., Weber and Ward, 2015), as well as in multibeam echosounders at a large incidence angle (e.g., Lurton, 2002, Fig. 8.30). Tracking the terminus position can provide a direct measurement of submerged terminus geometry, such as trends in the over- or undercutting of the submerged ice face (e.g., Weidner, 2025; Abib et al., 2023; Sutherland et al., 2019; Rignot et al., 2010; Robertson et al., 2012; Sugiyama et al., 2019).

In addition to observations of the submerged terminus, elevated backscattering from subglacial discharge can be seen in the echogram between 575 and 825 m along the transect. The geometry of the subglacial discharge evolves as it rises in the water column towards the surface. Initially, the region of elevated scattering extends outwards from the submerged terminus in a narrow core approximately 50 m across (620 to 675 m along the track), referred to here as the "plume" region following Mankoff et al. (2016). This plume extends 40 to 50 m outward from the ice face with little change in its along-track width (parallel to the ice face). At a range from the transducer of approximately 25 m, at 7 m depth, the plume

rapidly expands to a region more than 300 m across, referred to here as the "pool". The position and extent (distance along the calving front) of the surface expression of the subglacial discharge pool, observed from the deck of MV Ulla Rinman and in the time-lapse imagery, show agreement with the acoustic measurements. To our knowledge, these are the most detailed measurements, acoustic or otherwise, of the geometry of a subglacial discharge event. Measurements such as these can provide direct information about the variability in plume width, which strongly affects the plume neutral buoyancy depth, upwelling flux, and plume-driven renewal time (Slater et al., 2022). Future analysis could take advantage of split-aperture processing techniques employed for gas seep plumes (e.g., Blomberg et al., 2018; Jerram et al., 2015) to determine the position and geometry of the plume and submerged ice face more precisely.

Beyond spatial measurements of the discharge, broadband acoustic observations can elucidate the dynamics of sub-glacial discharge plumes, by acquiring data that reveal the scale and geometry of the discharge location at the grounding line. It is well established that fresh water from surface melting, precipitation events, and other terrestrial inputs is channeled upstream of the terminus and is injected into the fjord environment at the calving front; however, the nature of the discharge location, whether at single or multiple distinct locations (point source) or across the length of the terminus (line source) remains unclear (Jenkins, 2011; Mug-

ford and Dowdeswell, 2011; Xu et al., 2013, 2012). The geometry of the discharge location defines the plume evolution and, subsequently, the entrainment rate of ambient fjord water, the total area of enhanced submarine melt rates due to plume–ice interaction, and the spread of glacially modified waters at the depth of hydrostatic equilibrium (Motyka et al., 2003; Wagner et al., 2019). Moreover, geometry is an important component of the parameterization of plume dynamics for fjord-scale modeling (Cowton et al., 2015; Slater et al., 2020). Acoustic systems can provide direct observations of the subglacial discharge location, and the backscattering signal from the plume higher in the water column can provide important observations related to plume dynamics (e.g., entrainment rates and scale of overturning).

Acoustic observations from Hansbukta demonstrate that echosounders can verify the presence of subglacial discharge in the water column. In Hansbukta, the submerged expression of discharge coincided with a surface expression. Prior to this work, the detection of the presence of subglacial discharge plumes depended on the visible surface expression of sediment-laden waters (e.g., Chauché et al., 2014); however, at termini with deeper grounding lines, surface expression is not always expected (e.g., Stevens et al., 2016). Recent modeling work from Slater et al. (2022) indicates that only 28 % of subglacial discharge plumes in Greenland reach a neutral buoyancy in the photic zone due to a combination of nearterminus stratification and weak discharge. Thus, the Slater et al. (2022) results suggest that more than two-thirds of cases of plume dynamics are under-accounted for in modeling efforts of ice-ocean interactions, including increased submarine melt and calving rates; this does not even account for the fact that a plume reaching the photic zone does not guarantee that it will have a visible surface expression. Again, broadband echosounders offer the means to close these observational gaps, by providing remote verification of plume presence; to help better understand the dependency of plume dynamics on the slope of the submerged terminus (Jenkins, 2011); and to identify the plume neutral buoyancy depth, plume impact on downstream thermohaline structure, and plume and terminus geometry.

Any data collection, acoustic or otherwise, taking place in proximity to a tidewater glacier must consider the safety and logistical challenges associated with working in a hazardous, actively calving zone. Operations must define a minimum safety distance to protect the people, vessel, and equipment; this distance is strongly dependent on a number of parameters unique to the glacial system being studied. The minimum safety distance definition and the subsequent impact on acoustic data collection and analysis are discussed in detail in Sect. 5.4.

4.3 Quantitative mixing analysis and geophysical parameter estimation

To characterize the tidally driven mixing in Hansbukta, broadband acoustic observations were collected in tandem with measurements of dissipation rates, temperature variance (χ_T), and turbulent kinetic energy (ε) by the Epsifish in regions of stratified turbulence (Fig. 5). Comparison between broadband inversion measurements and the Epsifish ground-truth dataset illustrates the potential for accurate, remote, acoustically derived measurements of dissipation rates in high-latitude regions. Furthermore, the high-resolution echograms collected by broadband echosounder systems can image and quantify the evolution of shear instabilities associated with mixing over large regions.

The broadband acoustic-inversion method applied here has previously been leveraged to measure dissipation rates of turbulent kinetic energy in high-energy systems with intense salinity gradients in the Connecticut River (160-600 kHz; Lavery et al., 2013). In highly turbulent strongly stratified water columns, backscattering can be driven by small, random perturbations in density and compressibility brought about by fluctuations in the medium temperature and salinity associated with dynamic mixing (Goodman and Forbes, 1990). A theoretical acoustic scattering model for isotropic homogenous turbulent microstructure (Lavery et al., 2003) is used here and is outlined in detail in Appendix C. In short, the calibrated and corrected volumetric scattering derived from field observations is fit to the scattering model output, which is constrained by the in situ data collected by the Epsi-fish, which was < 150 m from the acoustic transect. Fitting the scattering model provides an acoustically derived measurement of the dissipation rate of TKE, ε .

The application of broadband acoustic inversion to remotely measure dissipation rate TKE was applied to the acoustic transect collected running from north to south into the main channel of Hornsund Fjord, the area of interest just outside the primary sill of Hansbukta (Fig. 1). The data were collected near the peak ebb tide, and the echogram shows elevated scattering associated with shear instabilities, thermohaline structure, and individual fish in the region of interest highlighted in Fig. 5, between 10 and 28 m depth. The vertical profiles of temperature and salinity from the coincident Epsi-fish cast show several pycnocline regions associated with glacially derived water mass, similar to the structure observed in Fig. 3 and discussed in Sect. 4.1. At the sharp thermocline at $\sim 16 \, \mathrm{m}$ depth, TKE and thermal dissipation rates observed from the Epsi-fish are elevated more than an order of magnitude above background levels. Elevated scattering is seen at the same location, associated with shear instabilities that evolve along the track into a breaking internal wave.

The dissipation rate of TKE can be measured from the backscattered signal with the help of a theoretical acoustic scattering model and direct sampling from the Epsi-fish. The

Epsi-fish measurements not only inform the acoustic scattering model but were also used to validate the acoustically derived measurements. The local temperature and salinity measured by the Epsi-fish (Fig. 5) were used to estimate the molecular kinematic viscosity (υ) , the saline contraction and thermal expansion coefficients $(\beta \text{ and } \alpha)$, the fractional change in sound speed due to temperature and salinity (a and b), and the mean gradients of salinity $(\partial \bar{S}/\partial z)$ and temperature $(\partial \bar{T}/\partial z)$. Together with peak values of the dissipation rate of TKE (ε) , the Epsi-fish measurements were used to

- 1. determine the turbulent energy regime of the broadband acoustic observations,
- 2. model the predicted frequency-dependent backscattering cross section (σ_v), and
- 3. validate our acoustically derived estimate of the dissipation rate of TKE (ε) .

The Epsi-fish measurements of the region of interest in Fig. 5 indicate that all of the acoustic observations fell well within the viscous–convective turbulent energy regime. As a result, the scattered energy from the turbulent mixing associated with the breaking internal wave, here referred to as the backscattering cross section (σ_v), could be computed following Eq. (6) from Lavery et al. (2013):

$$\sigma_{v}(f) = 2^{-3} f q \left(\frac{\varepsilon}{v}\right)^{-\frac{1}{2}} \frac{4\pi \varepsilon R_{F}}{cg\beta} \frac{\partial \bar{S}}{\partial z} \cdot \left(A^{2} \left(\frac{\partial \bar{T}/dz}{\partial \bar{S}/dz}\right)^{2} + B^{2} + 2AB \frac{\partial \bar{T}/dz}{\partial \bar{S}/dz}\right), \tag{1}$$

where f is the acoustic frequency (in kHz), evaluated over the range 160–240 kHz; q is a constant defined by Oakey (1982); c is the speed of sound; R_F is the non-dimensional Richardson flux number, defined by Osborn (1980) as 0.15; g is the gravitational constant; and A and B account for the fractional changes in sound speed and density due to temperature and salinity, such that $A = \alpha + a$ and $B = \beta b$. The full derivation for Eq. (1) is found in Appendix C.

Equation (1) was used to predict the broadband backscattering intensity spectra over the experimental frequency range (160–240 kHz) using the Epsi-fish measurement (Fig. 5). The Epsi-fish-derived predictions of the backscattering cross section were then compared to acoustically derived measurements of the backscattering cross section in the region of interest.

To compute $\sigma_{\rm v}(f)$, a time series with a length of 36 samples, approximately 0.28 ms, was extracted across 25 acoustic profiles. The Fourier transform of the profiles was taken to compute the frequency-dependent backscattering ($S_{\rm MF}$). The ensemble average backscattering cross section was computed from the ensemble of the extracted $S_{\rm MF}$ measurements following a modified form from Weber and Ward (2015):

$$\sigma_{\rm v}(f) = \frac{\langle |S_{\rm MF}(f)|^2 \rangle}{C(f)} \frac{r^4}{\exp\left(-4\alpha_a(f)r\right)} \frac{1}{V(f)}, \tag{2}$$

where the brackets $\langle \rangle$ specify an ensemble average over multiple acoustic profiles, C is the frequency-dependent main response axis (MRA) correction factor, r is the range to the region of interest, α_a is the frequency-dependent absorption coefficient (in neper m⁻¹), and V is the frequency-dependent ensonified area. The volumetric backscattering intensity, plotted in Fig. 5, is the logarithmic form of the backscattering cross section volumetric scattering, S_v , such that $S_v = 10\log_{10}(\sigma_v)$ (with units of dB re m⁻¹). An in-depth discussion of Eq. (2) can be found in Appendix B.

The analysis of the acoustic measurements can be expanded upon. For example, the measurements of the backscattering cross section can be inverted using Eq. (1) to directly, remotely estimate the dissipation rate of TKE. The model (Eq. 1) was rewritten to solve for the dissipation rate of TKE using both the ensemble average volume scattering measurements and the basic oceanographic measurements from the Epsi-cast, and it was then evaluated to provide a remote, acoustically derived measurement of the dissipation rate of TKE which can be compared to the Epsi-fish in situ measurement. This method is not without precedent; it has been successfully applied in the Connecticut River by Lavery et al. (2013) and in the Baltic Sea by Muchowski et al. (2022).

Before discussing the results of the broadband measurements of the frequency-dependent backscattering cross section and the resulting inversion estimating the dissipation rate of TKE, it is important to clarify the assumptions involved in this analysis. First, there is an approximately 150 m separation between the deployment location of the microstructure probe and the acoustic data shown in Fig. 5. Both data were taken approximately the same distance from the sill, but the measurements made by the Epsi-fish may not be representative of the water column sampled by the acoustic system, especially if mixing associated with the sill had spatial heterogeneity. Furthermore, the acoustic scattering model (Eq. 1) used in this analysis assumes that a homogenous, isotropic turbulent microstructure is responsible for the scattered signal, and any patchiness in that phenomenon is not accounted for in the model application. The short ranges associated with this analysis mean that the area sampled is relatively small, < 3 m³, and previous research (e.g., Muchowski et al., 2022), working in deeper conditions (larger sampled areas), has made the homogenous, isotropic assumption. Finally, the use of a single acoustic scattering model for inversion estimates assumes either a single or dominant scattering mechanism. It is always possible, indeed likely, that multiple scattering mechanisms are present in the sampled region at a given moment in time; however, this ambiguity can be broken by considering the broadband spectral response and comparing field measurements to the known frequency dependencies of various potential scattering mechanisms, as is done in the following paragraph.

There is excellent agreement between both the modeled predictions of volumetric scattering and the values of dis-

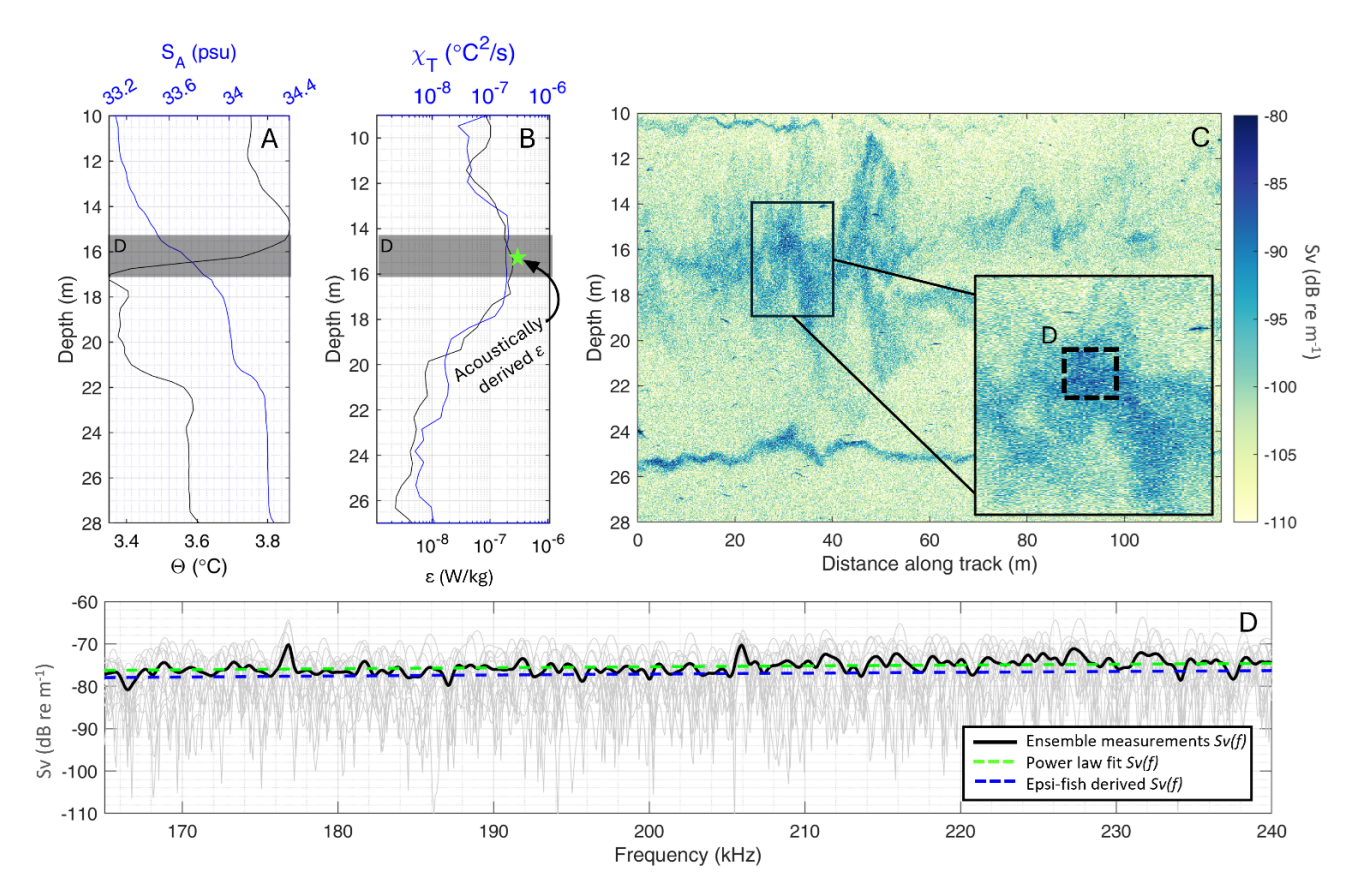


Figure 5. Combining Epsi-fish ground-truth and broadband acoustic data to better characterize mixing in the water column. Vertical profiles of temperature and salinity (**A**) as well as dissipation rates of temperature variance and turbulent kinetic energy (**B**) measured by the Epsi-fish cast. Panel (**C**) is an echogram of backscattering intensity (S_v) collected in close proximity (within 150 m) to the Epsi-fish cast. The inset box in panel (**C**) provides an enlarged view of the sampled region (dashed box marked **D**), from which $S_v(f)$ was calculated using Eq. (2) and is plotted in panel (**D**). The light-gray lines in panel (**D**) are the individual measurements of $S_v(f)$ from each sampled acoustic record, whereas the thick black line is the ensemble average of all records. The dashed green line is the power law fit of the ensemble $S_v(f)$ measurement, which was used to invert for ε . The acoustically derived ε is plotted in panel (**B**) (green star). The dashed blue line in panel (**D**) is the output of Eq. (1) evaluated with the Epsi-fish direct measurements, taken from the regions highlighted using the dark box in panels (**A**) and (**B**). See Fig. 1 (highlighted yellow transect lines and yellow marker) for the transect and Epsi-fish profile locations within the larger study site of Hansbukta.

sipation rate of TKE measured by the Epsi-fish cast and the acoustically derived observations as illustrated in Fig. 5. First, the acoustic field measurements of volume scattering from the region associated with the breaking internal wave show a weakly positive frequency dependence of f^1 , measured by least-squares fitting a power law distribution. This power law dependence is the same as that predicted by Eq. (1) for backscattering from a turbulent microstructure in the viscous-convective regime. While there are indications of other scattering mechanisms in the echogram (e.g., fish and thermohaline structure), neither have this power law spectra dependency; this, combined with Eq. (1) and the general context, suggests that the observed elevated scattering associated with the region centered at 16 m depth is driven by a turbulent microstructure. Here, the dissipation rate of TKE derived through acoustic inversion was measured to be 5.5×10^{-7} (W kg⁻¹), compared to the peak Epsifish measurement of 2.7×10^{-7} (W kg⁻¹). The close agreement, within a factor of 2, suggests that the acoustic method is viable and that the backscattering signal observed in the echogram surrounding the region of interest could be inverted to provide estimates of the dissipation rate of TKE over a larger area, leveraging the high-resolution nature of acoustic data to characterize mixing across the region.

Future work will expand the acoustically derived measurements to contextualize dissipation rate variability at the sill over various stages in the tidal cycle and over the subglacial discharge plume in the glacial trough. The highly resolved nature of broadband echograms, defined by both the individual acoustic profile depth resolution and the spacing of along-track profiles, means that we can extract measurements of dissipation rates at spatial scales unheard of with direct profile sampling equipment and use these high-resolution measurements to better inform mixing models in the highly dy-

namic high-latitude fjords; such information can improve our understanding of heat and salt transport across fjords. The fact that TKE dissipation rates can be obtained remotely is going to be a critical tool for understanding ablation mechanisms at the glacier terminus, where it is very difficult to obtain in situ measurements.

5 Considerations in the use of broadband active acoustic tools

Despite their many strengths, broadband acoustic systems are not generally used as a stand-alone observational tool, and the successful collection of quality data depends on thorough and well-defined mobilization, deployment, survey procedures, field processing, and data quality control and assessment methods. First, while split-beam transducers have straightforward deployment geometries and minimal positioning and motion data stream requirements in comparison to other types of active acoustic systems (e.g., multibeam echosounders), broadband transceivers are sensitive to external noise sources (e.g., other active acoustic systems, ship noise, and electrical interference). The successful collection of quality broadband water column data requires a wellconsidered mobilization plan for field activities, discussed in Sect. 5.1. Second, quantitative analysis, such as broadband spectral characterization or acoustic-inversion procedures, requires calibration of the echosounder and application of a series of corrections related to sound propagation and scattering. The post-processing pipeline for broadband data to account for these corrections remains a barrier for new users. Many research groups rely on processing tools developed in-house because of the lack of open-source commercial software. Techniques for processing are improving; several open-source data analysis tools have become available in recent years, such as EPS3 (Ladroit et al., 2023) and EchoPype (Lee et al., 2021). Commercial developers have tools to process narrowband data and have recently started to expand the processing capability to broadband systems. However, these software packages are costly and their broadband spectral analysis tools are still in the early stages of development. Section 5.2 covers the need to account for the underlying physics of sound propagation and the time and personnel budgets for these activities during field expeditions. The inherent ambiguity in acoustic observations briefly noted in Sect. 4 and the ongoing challenge with respect to interpreting all active acoustic data, no matter the quality of data collection, are discussed in Sect. 5.3. Finally, in Sect. 5.4, there is a discussion of the safety, data collection, and data quality considerations that come into play when making observations in proximity to the terminus of a tidewater glacier.

5.1 Noise considerations during deployment

Echosounders used in scientific applications have high receive sensitivity, which allows for the measurement of a wide frequency range of relatively low amplitude acoustic signals. High receive sensitivity, combined with pulse compression signal processing, enables the observation of weakly scattering phenomenon, such as thermohaline and mixing structure, as reported in Figs. 3-5; however, high receive sensitivity also makes broadband echosounders susceptible to external noise across a broad range of frequencies, from other acoustic systems (e.g., ship bottom pingers), environmental sources (e.g., wind and waves), ship noise, and electrical interference. From a practical perspective, any increase in interference with the received acoustic signal from external noise sources will reduce the signal-to-noise ratio of the system, resulting in a reduction in the range of detection of objects in the water column and broadband spectral characterization capabilities.

Vessel mobilization of the broadband transducers must consider equipment placement with respect to noise sources and flow structures, as well as transducer safety, to ensure the collection of quality data. Electrical noise, often caused by electromagnetic interference from ship-based power or voltage drops from high-current equipment, such as winches, commonly reduces the quality of acoustic data. Noise reduction measures must also be considered in the installation and acquisition procedures of the acoustic topside unit. When the EK80 wideband transceiver was acquiring acoustic data during the Hornsund Fjord expedition, the MV Ulla Rinman's ship sonar was turned off to remove the potential for crosstalk between the two systems. During the collection of in situ data, the broadband system did not acquire data, due to interference from the ship's winch, and at the completion of in situ data collection, the winch and all associated electronics were secured. Furthermore, the full suite of broadband echosounder equipment (e.g., transducer, transceiver, positioning system, and acquisition laptop) was run from a separate marine-grade battery, due to electrical noise associated with ship power. Moreover, the ES200-7CD split-beam transducer was deployed from a side-mounted pole on the forward, starboard side of MV Ulla Rinman. The side-mounted pole was a total of 6 m in length, with 2 m sitting below the water line to protect the transducer from interaction with surface ice mélange. The location of the pole was selected to minimize vibrations and the impact of bubbles entrained by the vessel to help minimize noise and performance degradation. Additionally, the pole location on MV Ulla Rinman also allowed (1) the field team to maintain visual contact during survey activities from the ship's bridge and (2) easy access for regular pole deployment and acoustic calibration procedures. Installation of the transducer must ensure as close to a laminar water flow over the transducer face as possible, as any vibration will be converted into electrical energy, contributing to the background noise level.

5.2 Acoustic corrections in post-processing

The successful interpretation of acoustic data relies upon the accurate and thoughtful application of corrections in the post-processing pipeline. Appropriate corrections are dependent on the type of analysis but typically include the application of a calibration offset to account for the accuracy and precision in signal transduction and measurements, geometric spreading corrections, and frequency-dependent absorption estimations (see Eq. 2).

Acoustic instruments need to be calibrated frequently, as their performance will change with the deployment environment and over the life of the instrument (Demer and Hewitt, 1993; Brierley et al., 1998; Nam et al., 2007). It is best practice to calibrate a system over the range of environmental conditions encountered when measurements are made; water temperature is of particular concern for high-latitude work. Calibration methods for split-beam echosounders are well defined in the literature and are described in detail in Demer et al. (2015). In short, a small (< 50 mm) sphere of known physical properties is hung in the beam of the acoustic transducer on the experiment platform and moved throughout the acoustic beam, where its position is determined through split-aperture processing to measure variability in sensitivity. The expected backscattering from the sphere is calculated using a theoretical model for the reflection of sound by elastic spheres (MacLennan, 1981) and is compared to the measurements made in the field. The resulting calibration offset, for example C(f) in Eq. (2), adjusts the gain and filter attenuation correction factor of echosounder measurements, as well as correcting for frequency-dependent beamwidth and receive sensitivity inherent to broadband echosounders (Rogers and Van Buren, 1978).

Beyond calibration offsets, all quantitative acoustic analysis must account for the frequency-dependent absorption of acoustic energy by the propagation medium and the geometric spreading of the acoustic signal. Acoustic absorption refers to the gradual loss of energy due to interaction with water molecules and dissolved substances. Absorption is a function of both seawater properties (e.g., temperature and salinity) and frequency, and it is corrected for in logarithmic space for frequencies between 160 and 240 kHz (in dB m⁻¹) (Francois and Garrison, 1982). Geometric spreading refers to the propagation of the broadband signal outward in all directions from the transducer, resulting in a rangedependent loss of acoustic energy for a given area. Depending on the underlying physics of the scattering phenomena in question, geometric spreading can be accounted for with different range-dependent corrections, the most common being spherical spreading correction, but other corrections may be more appropriate depending on the circumstances.

5.3 Ambiguity in the backscattered signal

Observations made by active acoustic systems are inherently ambiguous, as scattering in the water column can be associated with multiple dynamics and visually differentiating between processes is not always possible. The correct interpretation of backscattering signals requires an understanding of how acoustic systems work and proper application of corrections for sound propagation and scattering associated with targets, like those discussed in Sect. 5.2. In circumstances where these steps are skipped, the potential for inaccurately identifying water column processes and mis-quantifying geophysical parameters is high.

As discussed in Sect. 4.3, broadband spectral analysis combined with theoretical acoustic scattering models can differentiate between scattering mechanisms; however, direct measurements remain an essential and straightforward tool to inform and contextualize remote acoustic observations. Field procedures should plan to include co-located in situ sampling when possible; these data can provide context and clarity to the acoustic observations, as illustrated in Sect. 4.1, as well as inform theoretical acoustic scattering models to assist in broadband spectral analysis, as in Sect. 4.3.

The application of acoustic scattering models to explain broadband spectral characteristics or assist with acousticinversion methods also requires forethought and experience. Many broadband inversion methods have been developed to apply to cases in which one scattering mechanism dominates the ensonified volume, e.g., sizing gas bubbles (Weidner et al., 2019), estimating rates of TKE dissipation in a highly stratified estuary (Lavery et al., 2013). In these cases, acoustic-inversion procedures are constrained by the nature of the sampled volume, as well as by the number of free parameters in the theoretical acoustic scattering model and the quality of the in situ sampling. Water column scattering is often associated with multiple dynamics, i.e., entrained gas bubbles associated with regions of intense mixing (Marston et al., 2023). When there is no dominant scatterer in the ensonified volume, inversion efforts are limited by the unknown combination scattering from multiple phenomena and the under-sampled nature of the inversion problem. Such issues can be overcome with knowledge of the study site, quality ground-truth data, and well-defined theoretical acoustic scattering models (e.g., Loranger et al., 2022; Lavery et al., 2010).

All considerations combined, users of broadband splitbeam echosounders should be prepared to refine deployment methodologies and employ noise reduction procedures to ensure the collection of high-quality acoustic data. Upon fieldwork completion, users should take the time to properly calibrate and correct data prior to analysis. Finally, users should carefully select and apply theoretical acoustic scattering models based on the best knowledge of data and model limitations for accurate and meaningful results.

5.4 Safety considerations near glacial termini

Calving events, above and below the waterline, create a dangerous environment in proximity to the ice-ocean interface of tidewater glaciers. Falling or surfacing ice and the resulting surface waves pose serious dangers near the calving front. As noted earlier, there is a paucity of observations in this region due to safety concerns, which preclude direct, ship-based sampling (e.g., deployment of sensors and water sampling). In Sect. 4.2, we discussed the use of broadband scientific echosounders to fill observational gaps by making remote measurements of this region, using data collected at Hansbreen as an example. However, the broader deployment of scientific echosounders for the study of submerged glacial termini and the proximal water column requires several important safety considerations, which in turn have implications for data collection and quality. Ship-based acoustic measurements of the ice-ocean interface must be made at a minimum safe distance (MSD) from the calving front. The MSD will vary by glacier but is generally $\sim 200 \, \mathrm{m}$ and accounts for the height of the ice cliff above the water line, the fjord topography and bathymetry, and the calving rate (Kohler, 2009). In fjords that are narrow or shallow, or have ice cliffs higher than 40-50 m, the MSD can be upwards of 500 m or more.

An extended MSD can impact the successful use of scientific echosounders for high-latitude studies and must be considered prior to field operations. The broadband transducer highlighted in this paper, the Simrad ES200-7CD, has a maximum useable range of approximately 250 m, beyond which signal attenuation reduces the signal-to-noise ratio below useable levels. However, signal attenuation is primarily driven by the frequency of the acoustic pulse, and several lower-frequency systems could be used to extend the data collection range to beyond 700 m. Increased distance between the acoustic transducer and the ice face also results in an increased observational area, defined by the acoustic beam footprint (e.g., the transducer beamwidth). An increased acoustic footprint limits the study of closely spaced phenomenon, such as individual bubbles, fish, or small-scale surface roughness of the ice face, but allows for a larger observational area.

Overall, the feasibility of deploying broadband scientific echosounders for the study of the ice—ocean interface of tidewater glaciers will be highly dependent on the glacier in question. Deploying a high-frequency (> 200 kHz) scientific echosounder on an operator-run vessel may not be feasible in cases where the MSD is large (> 200 m). In such cases, other deployment platforms could be considered, such as an uncrewed surface vehicle (USV), which can reduced the range between the transducer and submerged ice face. However, it is worth noting that integration of an acoustic system onto an USV can be complicated and will increase the cost of the deployment beyond what has been quoted in this paper.

6 Conclusions

Broadband split-beam scientific echosounders are a remotesensing tool particularly well suited for field deployment in high-latitude fjords. The high rate of acoustic profile collection and resulting data resolution is unmatched in comparison to traditional direct sampling. Broadband echograms provide illumination of the evolution of numerous scattering phenomena in the water column, including shear instabilities associated with bathymetry and tidally forced mixing, biological scattering from fish aggregations, and evolving thermohaline structure. As illustrated in this work, these observations can be used to contextualize water column dynamics over the full-fjord scale, remotely characterize processes occurring in dangerous or inaccessible locations (e.g., the submerged terminus), and provide geophysical measurements of water column processes through broadband spectral inversion when combined with in situ sampling and theoretical scattering models. Looking beyond the analysis discussed in this work, broadband split-beam systems have a history in the study of biophysical interactions (e.g., Benoit-Bird et al., 2009; Lavery et al., 2010), seafloor emission characterization (e.g., Loranger and Weber, 2020; Weidner et al., 2019), and sea ice (Bassett et al., 2020). The prospects for future studies of high-latitude glacial fjords with broadband systems are excellent, as they can improve observational capabilities in isolated and challenging field locations through the collection of qualitative images and quantitative measurements.

Tracking the spatiotemporal variability in fjord-scale thermohaline structure and quantifying dissipation rates will help characterize the relative importance of tidal forcing on heat, salt, and freshwater budgets in the highly dynamic high-latitude fjords like Hornsund Fjord. Concurrently, at the terminus of Hansbreen, split-aperture processing techniques have been employed to precisely determine the position and morphology of the submerged ice face (Weidner, 2025). These measurements will be combined with terrestrial laser scans to explore calving regimes above and below the waterline at Hansbreen.

Broadband echosounders are available to the oceanographic community from commercial sources. The start-up cost is approximately USD 80 000 (EUR 78 000) for the transducer, transceiver, and license to operate, and many systems are portable, with flexible deployment geometries and mobilization needs, making them an appealing tool for fieldwork when time and space are limited. Furthermore, many research vessels, including those operating in polar regions, are already equipped with split-beam narrowband sonar systems that can be upgraded with broadband capability at minimal cost. The application of broadband echo sounders in polar regions could, thus, enable an improved understanding of the complex geophysical dynamics of high-latitude fjords.

Appendix A: Equipment field mobilization and data collection procedures

Mobilization and calibration of the broadband acoustic system and other sampling equipment on MV Ulla Rinman took place on 5-6 July 2023. The acoustic system was operated continuously during survey operations in broadband mode. The transmit power was set to 150 W, and the pulse length was set to 1.012 ms. During mobilization, the acoustic system was calibrated with a 25 mm tungsten-carbide sphere following the well-documented procedure from Demer et al. (2015) in the western channel of Burgerbukta in Hornsund Fjord. The location was protected from swell and winds in the main channel of Hornsund Fjord and was calm and ice-free during calibration operations. A CTD cast was taken prior to calibration to characterize the water column properties. Field calibration results were compared to a post-expedition laboratory calibration which took place in the engineering tank at the University of New Hampshire on 13 March 2024, with the same acoustic equipment. Beam pattern characterization and broadband spectral power calibration results from the field and lab agreed, confirming the health of the transducer and calibration offset values applied in post-processing.

The Valeport miniCTD unit and the Epsi-fish microstructure probe were used for in situ water column sampling and were mobilized on 6 July 2023. The miniCTD unit was deployed from the starboard aft of MV *Ulla Rinman* on the upper level via the ship's winch. The winch provided a downward velocity of approximately $30\,\mathrm{cm\,s^{-1}}$. The miniCTD sensor went through a $30\,\mathrm{s}$ initialization procedure at 1 m depth prior to the cast. The Epsi-fish was deployed from the starboard aft of MV *Ulla Rinman* via a commercial fishing reel with a controlled descent rate of $\sim 0.6\,\mathrm{m\,s^{-1}}$. Time-lapse imagery was collected with two GoPro HERO11 cameras, which were deployed from the bridge deck and the transducer pole off the starboard side.

Acoustic survey activities took place between 7 and 12 July 2023 and consisted of approximately 80 km of broadband acoustic water column data, 40 CTD profiles, and 7 microstructure casts. During acoustic survey work, the MV *Ulla Rinman* vessel speed was limited to between 2 and 3 knots ($\sim 1\text{--}1.5~\mathrm{m\,s^{-1}}$), to maintain acoustic data density. Acoustic system parameters and direct sampling deployment procedures were kept consistent throughout survey activities.

The downward-looking geometry was employed to collect a series of north–south transects. The north–south transects were approximately 5 km long. All transects were run in pairs. The first transect was run continuously from the mouth of Hansbukta to the terminus of Hansbreen, collecting broadband acoustic data only. This provided continuous, uninterrupted acoustic observations of water column dynamics at the full-fjord scale. The second transect was run in the reciprocal direction, and acoustic data were collected, interspersed with ground-truth data collection at specific locations: near

the terminus of Hansbreen, in the glacial trough before the first set of sills, at the terminal moraine (shallowest sill), and in the main channel of Hornsund Fjord at the mouth of Hansbukta. North—south transects, along with ground-truth measurements, were collected in Hansbukta during multiple sections of the tidal cycle to capture the potential effect of tidal influence on mixing across the fjord. The tides in Hornsund Fjord are semidiurnal, with two low and high tides of approximately equal magnitude and a total tidal range generally between 2 and 3 m. Transect timing was determined using predicted tidal data from the Longyearbyen tidal station. In post-processing, the tidal phase was determined from the sea surface height measured by a pressure sensor from a mooring deployed in Hansbukta during survey operations.

The side-looking geometry was utilized to scan the iceocean interface of Hansbreen and remotely characterize processes occurring at the terminus. The geometry of the transducer mount setup provided a tilted beam geometry to collect observations of the near-terminus water column and the ice-ocean interface along a diagonal trajectory. The acoustic beam intersected with the submerged terminus between 15 and 25 m below the surface, depending on the distance between the ship and the ice face, which was not more than 200 m. The area ensonified was between 2.5 and 8.5 m². Survey lines were run from east to west, as the side-mount pole was on the starboard side of MV Ulla Rinman. During the survey, there was minimal ice mélange, which allowed for the same parallel track to be run several times. Parallel transects included the collection of CTD profiles and time-lapse photos. The CTD profile locations were chosen based on the subglacial discharge plume location, as observed in the acoustic data.

Appendix B: General flow of acoustic processing

All acoustic data presented in this paper are plotted as the volume backscattering intensity, $S_{\rm v}$, which has logarithmic units of decibels relative to 1/m and is computed as $S_{\rm v}=10\log_{10}\sigma_{\rm v}$, defined below in Eqs. (B1)–(B4). Volume backscattering intensity is a measure of the distributed scattering strength normalized by acoustic beam volume, which increases with increasing range from the transducer. The computation of $S_{\rm v}$ has the following steps: (1) application of the matched filter, (2) sampling of the acoustic time series, (3) range-dependent corrections for signal attenuation from spherical spreading and absorption, (4) calibration offset and beam volume correction application, and (5) corrections for vessel motion. Steps 1–4 are described in greater detail below.

The $S_{\rm v}$ computation is based on well-defined matchedfilter processing procedures (e.g., Weber and Ward, 2015; Lavery et al., 2017; Andersen et al., 2024), and for this work, it is calculated by modifying the seafloor scattering intensity, $\sigma(f)$, from Weber and Ward (2015), starting with Eq. (9):

$$\sigma\left(f\right) = \langle \left|S(f)\right|^{2} \rangle \frac{1}{C(f)} \frac{r^{4}}{\exp\left(-4\alpha(f)r\right)} \frac{1}{A}. \tag{B1}$$

Equation (B1) reports scattering by the statistics of an ensemble of realizations, $\langle \rangle$, of individual seafloor scattering observations, $|S|^2$. The C in the second term is the main response axis (MRA) correction factor. The third term represents a combination of spherical spreading losses and absorption, where a is the frequency-dependent absorption coefficient (in units of nepers m⁻¹) and r is the range between the region of interest (in meters) and the transmitter/receiver. Finally, scattering is corrected for the ensonified area of the seafloor in question, A (in m²).

In this paper, Eq. (B1) is modified to consider a region of scattering from a volume in the water column, rather than an area on the seafloor, resulting in measurements of volume backscattering intensity, $S_{\rm v}$. The ensemble realizations of scattering observations and corrections from the second and third terms of Eq. (B1) remain the same; however, the fourth term becomes a correction for beam volume, rather than area. For broadband spectra analysis (Sect. 4.3, Fig. 5), the modified equation takes the following form:

$$\sigma_{\rm v}(f) = \frac{\langle |S_{\rm MF}(f)|^2 \rangle}{C(f)} \frac{r^4}{\exp(-4\alpha(f)r)} \frac{1}{V(f)},\tag{B2}$$

where terms have the same definitions as Eq. (B1), except V which is the frequency-dependent ensonified area. The frequency-dependent scattering of water column observations, $S_{\rm MF}(f)$, is computed from the Fourier transform of the base-banded, matched-filtered output ($s_{\rm MF}$). The matched filter enhances the resolution and detection of water column targets and maximizes the signal-to-noise ratio (SNR). $s_{\rm MF}$ is computed from the summed signal from all four quadrants of the split-beam transducer, s(t), and an idealized transmit pulse, $s_{\rm I}(t)$, as follows:

$$s_{\text{MF}}(t) = \frac{s(t) \otimes s_{\text{I}}(t)^*}{|s_{\text{I}}(t)|^2}.$$
(B3)

The frequency-dependent ensonified volume can be approximated as a cylinder (see Fig. 3.17 in Lurton, 2002), defined by the range from the transducer to the region of interest, and the two-way equivalent beam angle. *V* can be calculated using the following expression (Eq. 3.44 in Lurton, 2002):

$$V(f) = \Psi(f)r^2 \frac{cT}{2},\tag{B4}$$

where T is the length (in seconds) of the analysis window, r is the range to the center of the region of interest (c(t - T/2)/2), c is the speed of sound, and $\Psi(f)$ is the frequency-dependent two-way equivalent beam angle (in steradians), as defined in Jech et al. (2005):

$$\Psi(f) = \int_{-\pi}^{\pi} \int_{0}^{\pi} b_{t}(\theta, \phi) b_{r}(\theta, \phi) \sin\theta d\theta d\phi,$$
 (B5)

where $b_{\rm t}$ and $b_{\rm r}$ are the acoustic transmitter and receiver beam pattern, respectively, and θ and ϕ are polar spherical coordinates.

To produce high-resolution echograms (Sect. 4.1–4.2, Figs. 3, 4), we consider the volume backscattering intensity in the time domain, rather than the frequency domain, and σ_v is defined as follows:

$$\sigma_{\rm v}(t) = \frac{|s_{\rm MF}(t)|^2}{C} \frac{r^4}{\exp(-4\alpha r)} \frac{1}{V},$$
 (B6)

where corrections for absorption and the main response axis (MRA) correction factor are evaluated at the nominal center frequency of the transducer, 200 kHz, and the time-domain matched-filtered output ($s_{\rm MF}$) from Eq. (3) is used directly to compute $\sigma_{\rm v}$. In the time domain, the ensonified volume can be approximated as a cylinder defined by the range from the transducer to the region of interest and the -3 dB beam angle ($\theta_{\rm 3\,dB}$) provided by the manufacturer:

$$V = \tan(\theta_{3 \, \text{dB}}) \, r \, \frac{c \tau_{\text{eff}}}{2}, \tag{B7}$$

where τ_{eff} is the effective pulse length (in seconds). Equation (B4) can also be used to compute the ensonified volume for a time-domain correction by modifying Eq. (B5) to compute the two-way equivalent beam angle at the nominal center frequency of the transducer.

For additional information on acoustic data processing steps and the computation of volumetric scattering intensity, we refer readers to Lavery et al. (2017) and Andersen et al. (2024) for alternative derivation and formulations of Eqs. (B2) and (B6), as well as additional explanation of broadband acoustic signal processing and calibration corrections.

Appendix C: Theoretical acoustic scattering model for turbulent microstructure

The wavenumber spectra for temperature and salinity are separated into three wavenumber regimes in the isotropic, homogenous turbulence model from Batchelor (1959). The measurements made in Hornsund Fjord with the ES200-7CD echosounder are limited to the viscous–convective subrange. In the viscous–convective regime, the 1D wavenumber spectra for temperature are given by Lavery et al. (2013) (Eq. 2):

$$\phi_{T,S} = q \chi_{T,S} \left(\frac{\varepsilon}{v}\right)^{-1} k^{-1}. \tag{C1}$$

Their co-spectra are given by the following:

$$\phi_{T-S} = q(\chi_T \chi_S)^{\frac{1}{2}} \left(\frac{\varepsilon}{\upsilon}\right)^{-\frac{1}{2}} k^{-1},\tag{C2}$$

where k is the wavenumber (m⁻¹); q is a dimensionless constant, defined by Oakey (1982) at q = 3.7; $\chi_{T,S}$ represents

the dissipation rates of temperature and salinity variance (${}^{\circ}\text{C}^2 \, \text{s}^{-1} \, \text{PSU}^2 \, \text{s}^{-1}$); υ is the molecular viscosity ($\text{m}^2 \, \text{s}^{-1}$); and ε is the dissipation rate of TKE (W kg⁻¹).

The scattering cross section per unit volume from homogeneous and isotropic fluctuations in temperature and salinity is given by Lavery et al. (2003) (Eq. 23) as follows:

$$\sigma_{\rm v}(k) = -\frac{k^4}{K} \left(A^2 \frac{\partial \phi_T(K)}{\partial k} + B^2 \frac{\partial \phi_S(K)}{\partial k} + 2AB \frac{\partial \phi_{T-S}(K)}{\partial k} \right), \tag{C3}$$

where A and B are terms that represent the fractional change in sound speed and density due to temperature and salinity changes. For the backscattering case in this article, the wavenumber spectra in Eq. (C2) are evaluated at the Bragg wavenumber (K = 2k).

$$\sigma_{v}(k) = 2^{-3}kq \left(\frac{\varepsilon}{v}\right)^{-\frac{1}{2}} \left(A^{2}\chi_{T} + B^{2}\chi_{S} + 2AB(\chi_{T}\chi_{S})^{\frac{1}{2}}\right)$$
 (C4)

The final expression for backscattering cross section per unit volume is derived by assuming that the dissipation rates of temperature and salinity are related to the mean gradients in water column properties,

$$\chi_S = \chi_T \left(\frac{\partial \bar{S}}{\partial \bar{T}} \right)^2, \tag{C5}$$

and that the dissipation rates of salinity and TKE can be related through the Richardson flux number (R_F) given by

$$R_{\rm F} = \frac{g\beta}{2\varepsilon\chi_S} \left(\frac{\partial\bar{S}}{\partial z}\right)^{-1},\tag{C6}$$

where β is the fractional change in density from salinity. Equations (C5) and (C6) are plugged into Eq. (C4) to provide the following expression for σ_v :

$$\begin{split} \sigma_{\rm v}(k) &= 2^{-3} kq \left(\frac{\varepsilon}{\upsilon}\right)^{-\frac{1}{2}} \frac{2\varepsilon R_{\rm F}}{g\beta} \frac{\partial \bar{S}}{\partial z} \\ &\cdot \left(A^2 \left(\frac{\partial \bar{T}}{\partial \bar{S}}\right)^2 + B^2 + 2AB \frac{\partial \bar{T}}{\partial \bar{S}}\right), \end{split} \tag{C7}$$

which is used in the analysis to match the broadband spectral measurements of the breaking internal wave.

Data availability. The data that support the findings of this work are available at https://doi.org/10.6075/J0N87B1B (Weidner and Deane, 2024) as part of the University of California San Diego Library Digital Collections. Information on the Polish Polar Station Hornsund can be found at https://hornsund.igf.edu.pl/ (last access: 1 August 2025).

Author contributions. EW and GD designed the acoustic field campaign. EW, GD, MDS, HJ, HV, MC, and OG collected the dataset

in Hornsund Fjord. EW analyzed the data with assistance from GD, ALB, MA, and FS. EW prepared the manuscript with contributions from all co-authors.

Competing interests. The contact author has declared that none of the authors has any competing interests.

Disclaimer. Publisher's note: Copernicus Publications remains neutral with regard to jurisdictional claims made in the text, published maps, institutional affiliations, or any other geographical representation in this paper. While Copernicus Publications makes every effort to include appropriate place names, the final responsibility lies with the authors. Views expressed in the text are those of the authors and do not necessarily reflect the views of the publisher.

Acknowledgements. The authors thank the captain and crew of MV Ulla Rinman and the staff of the Polish Polar Station in Hornsund Fjord for making the field expedition possible. The authors are also grateful to Carlo Lanzoni at the Center for Coastal and Ocean Mapping for calibrating the acoustic equipment. We also thank Larry Mayer and Anthony Lyons at the University of New Hampshire for the loan of the broadband acoustic system used in this work. Research efforts were supported by the Office of Naval Research (award nos. N00014-23-1-2620, N00014-21-1-2304, and N00014-21-1-2316). Elizabeth Weidner was supported in this effort by a Scripps Institution of Oceanography postdoctoral fellowship. Hari Vishnu and Mandar Chitre were supported by the INTERACT III Transnational Access grant within the framework of the European Union H2020 program (grant no. 871120). Oskar Glowacki was supported by the National Science Centre, Poland (grant no. 2021/43/D/ST10/00616). We also thank the three anonymous reviewers for their comments which improved the content and readability of the manuscript.

Financial support. This research has been supported by the Office of Naval Research (grant nos. N00014-23-1-2620, N00014-21-1-2304, and N00014-21-1-2316), the Narodowym Centrum Nauki (grant no. 2021/43/D/ST10/00616), and the EU Horizon 2020 program (INTERACT III Transnational Access; grant no. 871120).

Review statement. This paper was edited by Elizabeth Bagshaw and reviewed by three anonymous referees.

References

Abib, N., Sutherland, D. A., Amundson, J. M., Duncan, D., Eidam, E. F., Jackson, R. H., Kienholz, C., Morlighem, M., Motyka, R. J., Nash, J. D., Ovall, B., and Pettit, E. C.: Persistent overcut regions dominate the terminus morphology of a rapidly melting tidewater glacier, Ann. Glaciol., 64, 1–12, https://doi.org/10.1017/aog.2023.38, 2023.

- Abib, N., Sutherland, D. A., Peterson, R., Catania, G., Nash, J. D., Shroyer, E. L., Stearns, L. A., and Bartholomaus, T. C.: Ice mélange melt changes observed water column stratification at a tidewater glacier in Greenland, The Cryosphere, 18, 4817–4829, https://doi.org/10.5194/tc-18-4817-2024, 2024.
- Amiri-Simkooei, A. R., Snellen, M., and Simons, D. G.: Principal Component Analysis of Single-Beam Echo-Sounder Signal Features for Seafloor Classification, IEEE Journal of Oceanic Engineering, 36, 259–272, https://doi.org/10.1109/JOE.2011.2122630, 2011.
- Andersen, L. N., Chu, D., Handegard, N. O., Heimvoll, H., Korneliussen, R., Macaulay, G. J., Ona, E., Patel, R., and Pedersen, G.: Quantitative processing of broadband data as implemented in a scientific split-beam echosounder, Meth. Ecol. Evol., 15, 317–328, https://doi.org/10.1111/2041-210X.14261, 2024.
- Bamber, J., van den Broeke, M., Ettema, J., Lenaerts, J., and Rignot, E.: Recent large increases in freshwater fluxes from Greenland into the North Atlantic, Geophys. Res. Lett., 39, https://doi.org/10.1029/2012GL052552, 2012.
- Bamber, J. L., Westaway, R. M., Marzeion, B., and Wouters, B.: The land ice contribution to sea level during the satellite era, Environ. Res. Lett., 13, 063008, https://doi.org/10.1088/1748-9326/aac2f0, 2018.
- Bassett, C., Lavery, A. C., Lyons, A. P., Wilkinson, J. P., and Maksym, T.: Direct inference of first-year sea ice thickness using broadband acoustic backscattering, J. Acoust. Soc. Am., 147, 824–838, https://doi.org/10.1121/10.0000619, 2020.
- Bassett, C., Lavery, A. C., Ralston, D., Geyer, W. R., Jurisa, J. T., Thomson, J., Honegger, D. A., Simpson, A., Scully, M. E., and Haller, M. C.: Acoustic backscattering at a tidal intrusion front, Prog. Oceanogr., 219, 103167, https://doi.org/10.1016/j.pocean.2023.103167, 2023.
- Batchelor, G. K.: Small-scale variation of convective quantities like temperature in a turbulent fluid, J. Fluid Mech., 5, 113–133, 1959.
- Beaird, N. L., Straneo, F., Le Bras, I., Pickart, R., and Jenkins, W. J.: Glacial Meltwater in the Current System of Southern Greenland, J. Geophys. Res.-Oceans, 128, e2023JC019658, https://doi.org/10.1029/2023JC019658, 2023.
- Bemis, K., Lowell, R. P., and Farough, A.: Diffuse Flow: On and Around Hydrothermal Vents at Mid-Ocean Ridges, Oceanography, 25, 182–191, 2012.
- Bendtsen, J., Mortensen, J., Lennert, K., and Rysgaard, S.: Heat sources for glacial ice melt in a west Greenland tidewater outlet glacier fjord: The role of subglacial freshwater discharge, Geophys. Res. Lett., 42, 4089–4095, https://doi.org/10.1002/2015GL063846, 2015.
- Benoit-Bird, K. J., Cowles, T. J., and Wingard, C. E.: Edge gradients provide evidence of ecological interactions in planktonic thin layers, Limnol. Oceanogr., 54, 1382–1392, https://doi.org/10.4319/lo.2009.54.4.1382, 2009.
- Björk, G., Jakobsson, M., Assmann, K., Andersson, L. G., Nilsson, J., Stranne, C., and Mayer, L.: Bathymetry and oceanic flow structure at two deep passages crossing the Lomonosov Ridge, Ocean Sci., 14, 1–13, https://doi.org/10.5194/os-14-1-2018, 2018.
- Błaszczyk, M., Jania, J. A., and Kolondra, L.: Fluctuations of tidewater glaciers in Hornsund Fjord (Southern Svalbard) since the

- beginning of the 20th century, Polish Polar Research, 34, 327–352, https://doi.org/10.2478/popore-2013-0024, 2013.
- Błaszczyk, M., Ignatiuk, D., Grabiec, M., Kolondra, L., Laska, M., Decaux, L., Jania, J., Berthier, E., Luks, B., Barzycka, B., and Czapla, M.: Quality Assessment and Glaciological Applications of Digital Elevation Models Derived from Space-Borne and Aerial Images over Two Tidewater Glaciers of Southern Spitsbergen, Remote Sens., 11, 1121, https://doi.org/10.3390/rs11091121, 2019.
- Błaszczyk, M., Jania, J.A., Ciepły, M., Grabiec, M., Ignatiuk, D., Kolondra, L., Kruss, A., Luks, B., Moskalik, M., Pastusiak, T., Strzelewicz, A., Walczowski, W., and Wawrzyniak, T.: Factors Controlling Terminus Position of Hansbreen, a Tidewater Glacier in Svalbard, J. Geophys. Res.-Earth Surf., 126, e2020JF005763, https://doi.org/10.1029/2020JF005763, 2021.
- Błaszczyk, M., Moskalik, M., Grabiec, M., Jania, J., Walczowski, W., Wawrzyniak, T., Strzelewicz, A., Malnes, E., Lauknes, T. R., and Pfeffer, W.: The Response of Tidewater Glacier Termini Positions in Hornsund (Svalbard) to Climate Forcing, 1992–2020, J. Geophys. Res.-Earth Surf., 128, e2022JF006911, https://doi.org/10.1029/2022JF006911, 2023.
- Blomberg, A. E. A., Weber, T. C., and Austeng, A.: Improved Visualization of Hydroacoustic Plumes Using the Split-Beam Aperture Coherence, Sensors, 18, 2033, https://doi.org/10.3390/s18072033, 2018.
- Böning, C. W., Behrens, E., Biastoch, A., Getzlaff, K., and Bamber, J. L.: Emerging impact of Greenland meltwater on deepwater formation in the North Atlantic Ocean, Nature Geosci., 9, 523–527, https://doi.org/10.1038/ngeo2740, 2016.
- Bourke, R. H. and Garrett, R. P.: Sea ice thickness distribution in the Arctic Ocean, Cold Reg. Sci. Technol., 13, 259–280. https://doi.org/10.1016/0165-232X(87)90007-3, 1987.
- Brierley, A. S., Goss, C., Watkins, J. L., and Woodroffe, P.: Variations in echosounder calibration with temperature, and some possible implications for acoustic surveys of krill biomass, CCAMLR Science, 5, 276–281, 1998.
- Burdic, W. S.: Underwater Acoustic System Analysis, 2nd edn., 328–331, Prentice Hall, Upper Saddle River, N. J., 1991.
- Chauché, N., Hubbard, A., Gascard, J.-C., Box, J. E., Bates, R., Koppes, M., Sole, A., Christoffersen, P., and Patton, H.: Iceocean interaction and calving front morphology at two west Greenland tidewater outlet glaciers, The Cryosphere, 8, 1457–1468, https://doi.org/10.5194/tc-8-1457-2014, 2014.
- Chu, D. and Stanton, T. K.: Application of pulse compression techniques to broadband acoustic scattering by live individual zooplankton, The Journal of the Acoustical Society of America, 104, 39–55, https://doi.org/10.1121/1.424056, 1998.
- Cotter, E., Murphy, P., Bassett, C., Williamson, B., and Polagye, B.: Acoustic characterization of sensors used for marine environmental monitoring, Marine Pollution Bulletin, 144, 205–215, https://doi.org/10.1016/j.marpolbul.2019.04.079, 2019.
- Cotter, E., Bassett, C., and Lavery, A.: Classification of broadband target spectra in the mesopelagic using physics-informed machine learning, The Journal of the Acoustical Society of America, 149, 3889–3901, https://doi.org/10.1121/10.0005114, 2021.
- Cottier, F., Tverberg, V., Inall, M., Svendsen, H., Nilsen, F., and Griffiths, C.: Water mass modification in an Arctic fjord through cross-shelf exchange: The seasonal hydrogra-

- phy of Kongsfjorden, Svalbard, J. Geophys. Res.-Oceans, 110, https://doi.org/10.1029/2004JC002757, 2005.
- Cowton, T., Slater, D., Sole, A., Goldberg, D., and Nienow, P.: Modeling the impact of glacial runoff on fjord circulation and submarine melt rate using a new subgrid-scale parameterization for glacial plumes, J. Geophys. Res.-Oceans, 120, 796–812, https://doi.org/10.1002/2014JC010324, 2015.
- Cummins, P. F., Armi, L., and Vagle, S.: Upstream Internal Hydraulic Jumps, J. Phys. Oceanogr., 36, 753–769, https://doi.org/10.1175/JPO2894.1, 2006.
- Ćwiąkała, J., Moskalik, M., Forwick, M., Wojtysiak, K., Giżejewski, J., and Szczuciński, W.: Submarine geomorphology at the front of the retreating Hansbreen tidewater glacier, Hornsund fjord, southwest Spitsbergen, J. Maps, 14, 123–134, https://doi.org/10.1080/17445647.2018.1441757, 2018.
- Demer, D. A. and Hewitt, R. P.: Calibration of an acoustic echointegration system in a deep tank, with gain comparisons over standard sphere material, water temperature and time, SC-CAMLR Selected Scientific Papers, 9, 127–144, 1993.
- Demer, D. A., Berger, L., Bernasconi, M., Bethke, E., Boswell, K., Chu, D., Domokos, R., Dunford, A., Fassler, S., Gauthier, S., Hufnagle, L. T., Jech, J. M., Bouffant, N., Lebourges-Dhaussy, A., Lurton, X., Macaulay, G. J., Perrot, Y., Ryan, T., Parker-Stetter, S., Stienessen, S., Weber, T., and Williamson, N.: Calibration of acoustic instruments, Report, International Council for the Exploration of the Sea (ICES), https://doi.org/10.25607/OBP-185, 2015.
- Demer, D. A., Andersen, L. N., Bassett, C., Berger, L., Chu, D., Condiotty, J. G. R. C., Hutton, B., Korneliussen, R., Bouffant, N. L., Macaulay, G., Michaels, W. L., Murfin, D., Pobitzer, A., Renfree, J. S., Sessions, T. S., Stierhoff, K. L., and Thompson, C. H.: 2016 USA–Norway EK80 Workshop Report: Evaluation of a wideband echosounder for fisheries and marine ecosystem science (report), ICES Cooperative Research Reports (CRR), https://doi.org/10.17895/ices.pub.2318, 2017.
- Ehrenberg, J. E. and Torkelson, T. C.: FM slide (chirp) signals: a technique for significantly improving the signal-to-noise performance in hydroacoustic assessment systems, Fish. Res., 47, 193–199, https://doi.org/10.1016/S0165-7836(00)00169-7, 2000.
- Enderlin, E. M. and Hamilton, G. S.: Estimates of iceberg submarine melting from high-resolution digital elevation models: application to Sermilik Fjord, East Greenland, J. Glaciol., 60, 1084–1092, https://doi.org/10.3189/2014JoG14J085, 2014.
- England, M. R., Eisenman, I., Lutsko, N. J., and Wagner, T. J. W.: The Recent Emergence of Arctic Amplification, Geophys. Res. Lett., 48, e2021GL094086, https://doi.org/10.1029/2021GL094086, 2021.
- Everett, A., Kohler, J., Sundfjord, A., Kovacs, K. M., Torsvik, T., Pramanik, A., Boehme, L., and Lydersen, C.: Subglacial discharge plume behaviour revealed by CTD-instrumented ringed seals, Sci. Rep., 8, 13467, https://doi.org/10.1038/s41598-018-31875-8, 2018.
- Farmer, D. and Armi, L.: Stratified flow over topography: the role of small-scale entrainment and mixing in flow establishment, P. Roy. Soc. Lond. A, 455, 3221–3258, https://doi.org/10.1098/rspa.1999.0448, 1999.
- Farmer, D. M. and Dungan Smith, J.: Tidal interaction of stratified flow with a sill in Knight Inlet, Deep-Sea Res. Pt. A, 27, 239–254, https://doi.org/10.1016/0198-0149(80)90015-1, 1980.

- Fichefet, T., Poncin, C., Goosse, H., Huybrechts, P., Janssens, I., and Le Treut, H.: Implications of changes in freshwater flux from the Greenland ice sheet for the climate of the 21st century, Geophys. Res. Lett., 30, https://doi.org/10.1029/2003GL017826, 2003.
- Fonseca, L. and Mayer, L.: Remote estimation of surficial seafloor properties through the application Angular Range Analysis to multibeam sonar data, Mar. Geophys. Res., 28, 119–126, https://doi.org/10.1007/s11001-007-9019-4, 2007.
- Francois, R. E. and Garrison, G. R.: Sound absorption based on ocean measurements: Part I: Pure water and magnesium sulfate contributions, Journal of the Acoustical Society of America, 72, 896–907, 1982.
- Geyer, W. R. and Ralston, D. K.: 2.03 The Dynamics of Strongly Stratified Estuaries, in: Treatise on Estuarine and Coastal Science, edited by: Wolanski, E. and McLusky, D., Academic Press, Waltham, 37–51, https://doi.org/10.1016/B978-0-12-374711-2.00206-0, 2011.
- Geyer, W. R., Ralston, D. K., and Holleman, R. C.: Hydraulics and mixing in a laterally divergent channel of a highly stratified estuary, J. Geophys. Res.-Oceans, 122, 4743–4760, https://doi.org/10.1002/2016JC012455, 2017.
- Geyman, E. C., van Pelt, J. J. W., Maloof, A. C., Aas, H. F., and Kohler, J.: Historical glacier change on Svalbard predicts doubling of mass loss by 2100, Nature, 601, 374–379, https://doi.org/10.1038/s41586-021-04314-4, 2022.
- Godø, O. R., Handegard, N. O., Browman, H. I., Macaulay, G. J., Kaartvedt, S., Giske, J., Ona, E., Huse, G., and Johnsen, E.: Marine ecosystem acoustics (MEA): quantifying processes in the sea at the spatio-temporal scales on which they occur, ICES Journal of Marine Science, 71, 2357–2369, https://doi.org/10.1093/icesjms/fsu116, 2014.
- Goodman, L.: Acoustic scattering from ocean microstructure, J. Geophys. Res.-Oceans, 95, 11557–11573, https://doi.org/10.1029/JC095iC07p11557, 1990.
- Goodman, L. and Forbes, M. J.: Acoustic scattering from ocean microstructure, J. Acoust. Soc. Amer., 87, S6, https://doi.org/10.1121/1.2028334, 1990.
- Grabiec, M., Ignatiuk, D., Jania, J. A., Moskalik, M., Głowacki, P., Błaszczyk, M., Budzik, T., and Walczowski, W.: Coast formation in an Arctic area due to glacier surge and retreat: The Hornbreen–Hambergbreen case from Spistbergen, Earth Surf. Process. Landf., 43, 387–400, https://doi.org/10.1002/esp.4251, 2018.
- Hager, A. O., Sutherland, D. A., Amundson, J. M., Jackson, R. H., Kienholz, C., Motyka, R. J., and Nash, J. D.: Subglacial Discharge Reflux and Buoyancy Forcing Drive Seasonality in a Silled Glacial Fjord, J. Geophys. Res.-Oceans, 127, e2021JC018355, https://doi.org/10.1029/2021JC018355, 2022.
- Holbrook, W. S., Páramo, P., Pearse, S., and Schmitt, R. W.: Thermohaline Fine Structure in an Oceanographic Front from Seismic Reflection Profiling, Science, 301, 821–824, https://doi.org/10.1126/science.1085116, 2003.
- Holland, D. M., Thomas, R. H., de Young, B., Ribergaard, M. H., and Lyberth, B.: Acceleration of Jakobshavn Isbræ triggered by warm subsurface ocean waters, Nature Geosci., 1, 659–664, https://doi.org/10.1038/ngeo316, 2008.
- Hopwood, M. J., Carroll, D., Browning, T. J., Meire, L., Mortensen, J., Krisch, S., and Achterberg, E. P.: Non-linear response of summertime marine productivity to increased melt-

- water discharge around Greenland, Nat. Commun., 9, 3256, https://doi.org/10.1038/s41467-018-05488-8, 2018.
- Hopwood, M. J., Carroll, D., Dunse, T., Hodson, A., Holding, J. M., Iriarte, J. L., Ribeiro, S., Achterberg, E. P., Cantoni, C., Carlson, D. F., Chierici, M., Clarke, J. S., Cozzi, S., Fransson, A., Juul-Pedersen, T., Winding, M. H. S., and Meire, L.: Review article: How does glacier discharge affect marine biogeochemistry and primary production in the Arctic?, The Cryosphere, 14, 1347–1383, https://doi.org/10.5194/tc-14-1347-2020, 2020.
- Howat, I. M., Joughin, I., and Scambos, T. A.: Rapid Changes in Ice Discharge from Greenland Outlet Glaciers, Science, 315, 1559–1561, https://doi.org/10.1126/science.1138478, 2007.
- Jackson, R. H., Nash, J. D., Kienholz, C., Sutherland, D. A., Amundson, J. M., Motyka, R. J., Winters, D., Skyllingstad, E., and Pettit, E. C.: Meltwater Intrusions Reveal Mechanisms for Rapid Submarine Melt at a Tidewater Glacier, Geophys. Res. Lett., 47, e2019GL085335, https://doi.org/10.1029/2019GL085335, 2020.
- Jakacki, J., Przyborska, A., Kosecki, S., Sundfjord, A., and Albretsen, J.: Modelling of the Svalbard fjord Hornsund, Oceanologia, 59, 473–495, https://doi.org/10.1016/j.oceano.2017.04.004, 2017.
- Jakobsson, M., Mayer, L. A., Nilsson, J., Stranne, C., Calder, B., O'Regan, M., Farrell, J. W., Cronin, T. M., Brüchert, V., Chawarski, J., Eriksson, B., Fredriksson, J., Gemery, L., Glueder, A., Holmes, F. A., Jerram, K., Kirchner, N., Mix, A., Muchowski, J., Prakash, A., Reilly, B., Thornton, B., Ulfsbo, A., Weidner, E., Åkesson, H., Handl, T., Ståhl, E., Boze, L.-G., Reed, S., West, G., and Padman, J.: Ryder Glacier in northwest Greenland is shielded from warm Atlantic water by a bathymetric sill, Commun. Earth Environ., 1, 1–10, https://doi.org/10.1038/s43247-020-00043-0, 2020.
- Jech, J. M., Foote, K. G., Chu, D., and Hufnagle, L. C. Jr.: Comparing two 38-kHz scientific echosounders, ICES J Mar Sci, 62, 1168–1179, https://doi.org/10.1016/j.icesjms.2005.02.014, 2005.
- Jech, J. M.: What can you do with twenty years of water column sonar data? Plenty!, The Journal of the Acoustical Society of America, 149, A61, https://doi.org/10.1121/10.0004515, 2021.
- Jech, J. M. and Michaels, W. L.: A multifrequency method to classify and evaluate fisheries acoustics data, Can. J. Fish. Aquat. Sci., 63, 2225–2235, https://doi.org/10.1139/f06-126, 2006.
- Jenkins, A.: Convection-Driven Melting near the Grounding Lines of Ice Shelves and Tidewater Glaciers, J. Phys. Oceanogr., 41, 2279–2294, https://doi.org/10.1175/JPO-D-11-03.1, 2011.
- Jerram, K., Weber, T. C., and Beaudoin, J.: Split-beam echo sounder observations of natural methane seep variability in the northern Gulf of Mexico, Geochem. Geophys. Geosyst., 16, 736–750, https://doi.org/10.1002/2014GC005429, 2015.
- Joughin, I., Abdalati, W., and Fahnestock, M.: Large fluctuations in speed on Greenland's Jakobshavn Isbræ glacier, Nature, 432, 608–610, https://doi.org/10.1038/nature03130, 2004.
- Joughin, I., Alley, R. B., and Holland, D. M.: Ice-Sheet Response to Oceanic Forcing, Science, 338, 1172–1176, https://doi.org/10.1126/science.1226481, 2012.
- Kilcher, L. F. and Nash, J. D.: Structure and dynamics of the Columbia River tidal plume front, J. Geophys. Res.-Oceans, 115, https://doi.org/10.1029/2009JC006066, 2010.

- Kohler, J.: How close should boats come to the fronts of Svalbard's calving glaciers?, Commissioned report, Governor of Svalbard, http://hdl.handle.net/11250/173174 (last access: 1 August 2025), 2009.
- Konik, M., Darecki, M., Pavlov, A. K., Sagan, S., and Kowalczuk, P.: Darkening of the Svalbard Fjords Waters Observed With Satellite Ocean Color Imagery in 1997–2019, Front. Mar. Sci., 8, https://doi.org/10.3389/fmars.2021.699318, 2021.
- Kosiba, A.: Some of Results of Glaciological Investigations in SW-Spitsbergen: Carried Out During the Polish I.G.Y. Spitsbergen Expeditions in 1957, 1958 and 1959, Państwowe Wydawn, Nauk, 1960.
- Kowalik, Z., Marchenko, A., Brazhnikov, D., and Marchenko, N.: Tidal currents in the western Svalbard Fjords, Oceanologia, 57, 318–327, https://doi.org/10.1016/j.oceano.2015.06.003, 2015.
- Ladroit, Y., Escobar-Flores, P. C., and Maurice, A.: ESP3: Fisheries acoustics data processing software, SourceForge [EPS3], https:// sourceforge.net/p/esp3/wiki/ESP3/ (last access: 1 August 2025), 2023
- Lavery, A. C., Schmitt, R. W., and Stanton, T. K.: High frequency acoustic scattering from turbulent oceanic microstructure: The importance of density fluctuations, J. Acoust. Soc. Amer., 114, 2685, https://doi.org/10.1121/1.1614258, 2003.
- Lavery, A. C., Chu, D., and Moum, J. N.: Measurements of acoustic scattering from zooplankton and oceanic microstructure using a broadband echosounder, ICES Journal of Marine Science, 67, 379–394, https://doi.org/10.1093/icesjms/fsp242, 2010.
- Lavery, A. C., Geyer, W. R., and Scully, M. E.: Broad-band acoustic quantification of stratified turbulence, The Journal of the Acoustical Society of America, 134, 40–54, https://doi.org/10.1121/1.4807780, 2013.
- Lavery, A. C., Bassett, C., Lawson, G. L., and Jech, J. M.: Exploiting signal processing approaches for broadband echosounders, ICES Journal of Marine Science, 74, 2262–2275, https://doi.org/10.1093/icesjms/fsx155, 2017.
- LeBlanc, L. R., Mayer, L., Rufino, M., Schock, S. G., and King, J.: Marine sediment classification using the chirp sonar, The Journal of the Acoustical Society of America, 91, 107–115, https://doi.org/10.1121/1.402758, 1992.
- Le Boyer, A., Alford, M. H., Couto, N., Goldin, M., Lastuka, S., Goheen, S., Nguyen, S., Lucas, A. J., and Hennon, T. D.: Modular, Flexible, Low-cost Microstructure Measurements: The Epsilometer, J. Atmos. Ocean. Tech., 38, 657–668, https://doi.org/10.1175/JTECH-D-20-0116.1, 2021.
- Lee, W., Mayorga, E., Setiawan, L., Majeed, I., Nguyen, K., and Staneva, V.: Echopype: A Python library for interoperable and scalable processing of water column sonar data for biological information, arXiv [preprint], arXiv:2111.00187, 2021.
- Leon, G. R., Sandal, G. M., and Larsen, E.: Human performance in polar environments, Journal of Environmental Psychology, 31, 353–360, https://doi.org/10.1016/j.jenvp.2011.08.001, 2011.
- Li, J., Roche, B., Bull, J. M., White, P. R., Leighton, T. G., Provenzano, G., Dewar, M., and Henstock, T. J.: Broadband Acoustic Inversion for Gas Flux Quantification – Application to a Methane Plume at Scanner Pockmark, Central North Sea, J. Geophys. Res.-Oceans, 125, e2020JC016360, https://doi.org/10.1029/2020JC016360, 2020.
- Lilly, D. K.: A Severe Downslope Windstorm and Aircraft Turbulence Event Induced by a Mountain Wave,

- J. Atmos. Sci., 35, 59–77, https://doi.org/10.1175/1520-0469(1978)035<0059:ASDWAA>2.0.CO;2, 1978.
- Loranger, S. and Weber, T. C.: Shipboard Acoustic Observations of Flow Rate From a Seafloor-Sourced Oil Spill, J. Geophys. Res.-Oceans, 125, e2020JC016274, https://doi.org/10.1029/2020JC016274, 2020.
- Loranger, S., Jech, M. J., and Lavery, A. C.: Broadband acoustic quantification of mixed biological aggregations at the New England shelf break, The Journal of the Acoustical Society of America, 152, 2319–2335, https://doi.org/10.1121/10.0014910, 2022.
- Lurton, X.: An Introduction to Underwater Acoustics: Principles and Applications, Springer Science & Business Media, Springer, Berlin, Heidelberg, ISBN 978-3-540-78480-7, 2002.
- Lydersen, C., Assmy, P., Falk-Petersen, S., Kohler, J., Kovacs, K. M., Reigstad, M., Steen, H., Strøm, H., Sundfjord, A., Varpe, Ø., Walczowski, W., Weslawski, J. M., and Zajaczkowski, M.: The importance of tidewater glaciers for marine mammals and seabirds in Svalbard, Norway, J. Marine Syst., 129, 452–471, https://doi.org/10.1016/j.jmarsys.2013.09.006, 2014.
- MacLennan, D. N.: The theory of solid spheres as sonar calibration targets, Scottish Fisheries Research, 22, 17 pp., 1981.
- Mankoff, K. D., Straneo, F., Cenedese, C., Das, S. B., Richards, C. G., and Singh, H.: Structure and dynamics of a subglacial discharge plume in a Greenlandic fjord, J. Geophys. Res.-Oceans, 121, 8670–8688, https://doi.org/10.1002/2016JC011764, 2016.
- Marston, T. M., Bassett, C., Plotnick, D. S., Kidwell, A. N., and Honegger, D. A.: Three-dimensional observations of tidal plume fronts in estuaries using a synthetic aperture sonar array, The Journal of the Acoustical Society of America, 154, 1124–1137, https://doi.org/10.1121/10.0020671, 2023.
- Martin, L. V., Stanton, T. K., Wiebe, P. H., and Lynch, J. F.: Acoustic classification of zooplankton, ICES J. Mar. Sci., 53, 217–224, https://doi.org/10.1006/jmsc.1996.0025, 1996.
- McGee, T. M.: The Use of Marine Seismic Profiling for Environmental Assessment1, Geophysical Prospecting, 38, 861–880, https://doi.org/10.1111/j.1365-2478.1990.tb01879.x, 1990.
- McLaren, A. S., Bourke, R. H., Walsh, J. E., and Weaver, R. L.: Variability in sea-ice thickness over the North Pole from 1958 to 1992, Geophysical Monograph Series, 85, 363–371, https://doi.org/10.1029/GM085p0363, 1994.
- Medwin, H.: In situ acoustic measurements of microbubbles at sea, J. Geophys. Res., 82, 971–976, https://doi.org/10.1029/JC082i006p00971, 1977.
- Medwin, H. and Clay, C. S.: Fundamentals of Acoustical Oceanography, Journal of physical oceanography, Academic Press, https://doi.org/10.1016/B978-0-12-487570-8.X5000-4, 1997.
- Mortensen, J., Bendtsen, J., Motyka, R. J., Lennert, K., Truffer, M., Fahnestock, M., and Rysgaard, S.: On the seasonal freshwater stratification in the proximity of fast-flowing tidewater outlet glaciers in a sub-Arctic sill fjord, J. Geophys. Res.-Oceans, 118, 1382–1395, https://doi.org/10.1002/jgrc.20134, 2013.
- Motyka, R. J., Hunter, L., Echelmeyer, K. A., and Connor, C.: Submarine melting at the terminus of a temperate tidewater glacier, LeConte Glacier, Alaska, U.S.A, Ann. Glaciol., 36, 57–65, https://doi.org/10.3189/172756403781816374, 2003.
- Moum, J. N., Farmer, D. M., Smyth, W. D., Armi, L., and Vagle, S.: Structure and Generation of Turbulence at Interfaces Strained by Internal Solitary Waves Propagating Shoreward over the Continental Shelf, J. Phys.

- Oceanogr., 33, 2093–2112, https://doi.org/10.1175/1520-0485(2003)033<2093:SAGOTA>2.0.CO;2, 2003.
- Muchowski, J., Umlauf, L., Arneborg, L., Holtermann, P., Weidner, E., Humborg, C., and Stranne, C.: Potential and Limitations of a Commercial Broadband Echo Sounder for Remote Observations of Turbulent Mixing, J. Atmos. Ocean. Tech., 39, 1985–2003, https://doi.org/10.1175/JTECH-D-21-0169.1, 2022.
- Mugford, R. I. and Dowdeswell, J. A.: Modeling glacial meltwater plume dynamics and sedimentation in high-latitude fjords, J. Geophys. Res.-Earth Surf., 116, https://doi.org/10.1029/2010JF001735, 2011.
- Nam, G. H., Cox, M. G., Harris, P. M., Robinson, S. P., Hayman, G., Beamiss, G. A., and Esward, T. J.: A model for characterizing the frequency -dependent variation in sensitivity with temperature of underwater acoustic transducers from historical calibration data, Measurement Science and Technology, 18, 1553, https://doi.org/10.1088/0957-0233/18/5/047, 2007.
- Nick, F. M., Vieli, A., Howat, I. M., and Joughin, I.: Large-scale changes in Greenland outlet glacier dynamics triggered at the terminus, Nature Geosci., 2, 110–114, https://doi.org/10.1038/ngeo394, 2009.
- Nilsen, F., Cottier, F., Skogseth, R., and Mattsson, S.: Fjord–shelf exchanges controlled by ice and brine production: The interannual variation of Atlantic Water in Isfjorden, Svalbard, Cont. Shelf Res., 28, 1838–1853, https://doi.org/10.1016/j.csr.2008.04.015, 2008.
- Oakey, N. S.: Determination of the Rate of Dissipation of Turbulent Energy from Simultaneous Temperature and Velocity Shear Microstructure Measurements, Journal of physical oceanography, 12, pp 256–270, 1982.
- Orr, M. H., Haury, L. R., Wiebe, P. H., and Briscoe, M. G.: Backscatter of high-frequency (200 kHz) acoustic wavefields from ocean turbulence, The Journal of the Acoustical Society of America, 108, 1595–1601, https://doi.org/10.1121/1.1286883, 2000.
- Osborn, T. R.: Estimates of the Local Rate of Vertical Diffusion from Dissipation Measurements, American Meteorological Society, 10, 83–89, 1980.
- Palinkas, L. A. and Suedfeld, P.: Psychological effects of polar expeditions, The Lancet, 371, 153–163, https://doi.org/10.1016/S0140-6736(07)61056-3, 2008.
- Penrose, J. D. and Beer, T.: Acoustic reflection from estuarine pycnoclines. Estuarine, Coast. Shelf Sci., 12, 237–249, https://doi.org/10.1016/S0302-3524(81)80122-3, 1981.
- Promińska, A., Falck, E., and Walczowski, W.: Interannual variability in hydrography and water mass distribution in Hornsund, an Arctic fjord in Svalbard, Polar Research, 2018.
- Proni, J. R. and Apel, J. R.: On the use of high-frequency acoustics for the study of internal waves and microstructure, J. Geophys. Res., 80, 1147–1151, https://doi.org/10.1029/JC080i009p01147, 1075
- Rignot, E., Koppes, M., and Velicogna, I.: Rapid submarine melting of the calving faces of West Greenland glaciers, Nature Geosci., 3, 187–191, https://doi.org/10.1038/ngeo765, 2010.
- Robertson, C. M., Benn, D. I., Brook, M. S., Fuller, L. C., and Holt, K. A.: Subaqueous calving margin morphology at Mueller, Hooker and Tasman glaciers in Aoraki/Mount Cook National Park, New Zealand, J. Glaciol., 58, 1037–1046, https://doi.org/10.3189/2012JoG12J048, 2012.

- Rogers, P. H. and Van Buren, A. L.: New approach to a constant beamwidth transducer, Journal of the Acoustical Society of America, 64, 38–43, 1978.
- Ross, T. and Lavery, A.: Laboratory observations of doublediffusive convection using high-frequency broadband acoustics, Exp. Fluids, 46, 355–364, https://doi.org/10.1007/s00348-008-0570-9, 2009.
- Ross, T. and Lueck, R.: Estimating turbulent dissipation rates from acoustic backscatter, Deep-Sea Res. Pt. I, 52, 2353–2365, https://doi.org/10.1016/j.dsr.2005.07.002, 2005.
- Rothrock, D. A. and Wensnahan, M.: The Accuracy of Sea Ice Drafts Measured from U.S. Navy Submarines, J. Atmos. Ocean. Tech., 24, 1936–1949, https://doi.org/10.1175/JTECH2097.1, 2007.
- Sawada, K., Furusawa, M., and Williamson, N. J.: Conditions for the precise measurement of fish target strength in situ, The Journal of the Marine Acoustics Society of Japan, 20, 73–79, https://doi.org/10.3135/jmasj.20.73, 1993.
- Schaffer, J., Kanzow, T., von Appen, W.-J., von Albedyll, L., Arndt, J. E., and Roberts, D. H.: Bathymetry constrains ocean heat supply to Greenland's largest glacier tongue, Nat. Geosci., 13, 227–231, https://doi.org/10.1038/s41561-019-0529-x
- Seim, H. E., Gregg, M. C., and Miyamoto, R. T.: Acoustic Backscatter from Turbulent Microstructure, J. Atmos. Ocean. Tech., 12, 367–380, https://doi.org/10.1175/1520-0426(1995)012<0367:ABFTM>2.0.CO;2, 1995.
- Serreze, M. C. and Francis, J. A.: The Arctic Amplification Debate, Clim. Change, 76, 241–264, https://doi.org/10.1007/s10584-005-9017-y, 2006.
- Serreze, M. C. and Stroeve, J.: Arctic sea ice trends, variability and implications for seasonal ice forecasting, Philos. T. Roy. Soc. A, 373, 20140159, https://doi.org/10.1098/rsta.2014.0159, 2015.
- Siegert, M., Alley, R. B., Rignot, E., Englander, J., and Corell, R.: Twenty-first century sea-level rise could exceed IPCC projections for strong-warming futures, One Earth, 3, 691–703, https://doi.org/10.1016/j.oneear.2020.11.002, 2020.
- Simmonds, J. and MacLennan, D. N.: Fisheries Acoustics: Theory and Practice, John Wiley & Sons, Blackwell Publishing Ltd, https://doi.org/10.1002/9780470995303, 2008.
- Simmons, S. M., Azpiroz-Zabala, M., Cartigny, M. J. B., Clare, M. A., Cooper, C., Parsons, D. R., Pope, E. L., Sumner, E. J., and Talling, P. J.: Novel Acoustic Method Provides First Detailed Measurements of Sediment Concentration Structure Within Submarine Turbidity Currents, J. Geophys. Res.-Oceans, 125, e2019JC015904, https://doi.org/10.1029/2019JC015904, 2020.
- Slater, D. A., Straneo, F., Das, S. B., Richards, C. G., Wagner, T. J. W., and Nienow, P. W.: Localized Plumes Drive Front-Wide Ocean Melting of A Greenlandic Tidewater Glacier, Geophys. Res. Lett., 45, 12350–12358, https://doi.org/10.1029/2018GL080763, 2018.
- Slater, D. A., Felikson, D., Straneo, F., Goelzer, H., Little, C. M., Morlighem, M., Fettweis, X., and Nowicki, S.: Twenty-first century ocean forcing of the Greenland ice sheet for modelling of sea level contribution, The Cryosphere, 14, 985–1008, https://doi.org/10.5194/tc-14-985-2020, 2020.
- Slater, D. A., Carroll, D., Oliver, H., Hopwood, M. J., Straneo, F., Wood, M., Willis, J. K., and Morlighem, M.: Characteristic Depths, Fluxes, and Timescales for Greenland's Tidewater Glacier Fjords From Subglacial Discharge-Driven Upwelling

- During Summer, Geophys. Res. Lett., 49, e2021GL097081, https://doi.org/10.1029/2021GL097081, 2022.
- Smyth, W. D. and Moum, J. N.: Three-dimensional (3d) Turbulence, in: Encyclopedia of Ocean Sciences, edited by: Steele, J. H., Academic Press, Oxford, 2947–2955, https://doi.org/10.1006/rwos.2001.0134, 2001.
- Stanton, T. K., Chu, D., Jech, J. M., and Irish, J. D.: New broadband methods for resonance classification and high-resolution imagery of fish with swimbladders using a modified commercial broadband echosounder, ICES Journal of Marine Science, 67, 365–378, https://doi.org/10.1093/icesjms/fsp262, 2010.
- Stevens, L. A., Straneo, F., Das, S. B., Plueddemann, A. J., Kukulya, A. L., and Morlighem, M.: Linking glacially modified waters to catchment-scale subglacial discharge using autonomous underwater vehicle observations, The Cryosphere, 10, 417–432, https://doi.org/10.5194/tc-10-417-2016, 2016.
- Straneo, F. and Cenedese, C.: The Dynamics of Greenland's Glacial Fjords and Their Role in Climate, Annu. Rev. Marine Sci., 7, 89–112, https://doi.org/10.1146/annurev-marine-010213-135133, 2015.
- Straneo, F. and Heimbach, P.: North Atlantic warming and the retreat of Greenland's outlet glaciers, Nature, 504, 36–43, https://doi.org/10.1038/nature12854, 2013.
- Straneo, F., Curry, R. G., Sutherland, D. A., Hamilton, G. S., Cenedese, C., Våge, K., and Stearns, L. A.: Impact of fjord dynamics and glacial runoff on the circulation near Helheim Glacier, Nature Geosci., 4, 322–327, https://doi.org/10.1038/ngeo1109, 2011.
- Stranne, C., Mayer, L., Weber, T. C., Ruddick, B. R., Jakobsson, M., Jerram, K., Weidner, E., Nilsson, J., and Gårdfeldt, K.: Acoustic Mapping of Thermohaline Staircases in the Arctic Ocean, Sci. Rep., 7, 15192, https://doi.org/10.1038/s41598-017-15486-3, 2017.
- Strzelewicz, A., Przyborska, A., and Walczowski, W.: Increased presence of Atlantic Water on the shelf south-west of Spitsbergen with implications for the Arctic fjord Hornsund, Prog. Oceanogr., 200, 102714, https://doi.org/10.1016/j.pocean.2021.102714, 2022
- Sugiyama, S., Minowa, M., and Schaefer, M.: Underwater Ice Terrace Observed at the Front of Glaciar Grey, a Freshwater Calving Glacier in Patagonia, Geophys. Res. Lett., 46, 2602–2609, https://doi.org/10.1029/2018GL081441, 2019.
- Sutherland, D. A. and Straneo, F.: Estimating ocean heat transports and submarine melt rates in Sermilik Fjord, Greenland, using lowered acoustic Doppler current profiler (LADCP) velocity profiles, Ann. Glaciol., 53, 50–58, https://doi.org/10.3189/2012AoG60A050, 2012.
- Sutherland, D. A., Jackson, R. H., Kienholz, C., Amundson, J. M., Dryer, W. P., Duncan, D., Eidam, E. F., Motyka, R. J., and Nash, J. D.: Direct observations of submarine melt and subsurface geometry at a tidewater glacier, Science, 365, 369–374, https://doi.org/10.1126/science.aax3528, 2019.
- Swift, C. T.: Passive microwave remote sensing of the ocean A review, Bound.-Lay. Meteorol., 18, 25–54, https://doi.org/10.1007/BF00117909, 1980.
- Thorne, P. D. and Hanes, D. M.: A review of acoustic measurement of small-scale sediment processes, Cont. Shelf Res., 22, 603–632, https://doi.org/10.1016/S0278-4343(01)00101-7, 2002.

- Thorne, P. D. and Hardcastle, P. J.: Acoustic measurements of suspended sediments in turbulent currents and comparison with insitu samples, The Journal of the Acoustical Society of America, 101, 2603–2614, https://doi.org/10.1121/1.418501, 1997.
- Thorne, P. D. and Hurther, D.: An overview on the use of backscattered sound for measuring suspended particle size and concentration profiles in non-cohesive inorganic sediment transport studies, Cont. Shelf Res., 73, 97–118, https://doi.org/10.1016/j.csr.2013.10.017, 2014.
- Thorpe, S. A.: Transitional phenomena and the development of turbulence in stratified fluids: A review, J. Geophys. Res.-Oceans, 92, 5231–5248, https://doi.org/10.1029/JC092iC05p05231, 1987.
- Turin, G.: An introduction to matched filters, IRE Transactions on Information Theory, 6, 311–329, https://doi.org/10.1109/TIT.1960.1057571, 1960.
- Vagle, S., Chandler, P., and Farmer, D. M.: On the dense bubble clouds and near bottom turbulence in the surf zone, J. Geophys. Res.-Oceans, 110, https://doi.org/10.1029/2004JC002603, 2005.
- van den Broeke, M. R., Enderlin, E. M., Howat, I. M., Kuipers Munneke, P., Noël, B. P. Y., van de Berg, W. J., van Meijgaard, E., and Wouters, B.: On the recent contribution of the Greenland ice sheet to sea level change, The Cryosphere, 10, 1933–1946, https://doi.org/10.5194/tc-10-1933-2016, 2016.
- van Haren, H. and Gostiaux, L.: A deep-ocean Kelvin-Helmholtz billow train, Geophys. Res. Lett., 37, https://doi.org/10.1029/2009GL041890, 2010.
- Wagner, T. J. W., Straneo, F., Richards, C. G., Slater, D. A., Stevens, L. A., Das, S. B., and Singh, H.: Large spatial variations in the flux balance along the front of a Greenland tidewater glacier, The Cryosphere, 13, 911–925, https://doi.org/10.5194/tc-13-911-2019, 2019.
- Walczowski, W.: Frontal structures in the West Spitsbergen Current margins, Ocean Sci., 9, 957–975, https://doi.org/10.5194/os-9-957-2013, 2013.
- Walczowski, W. and Piechura, J.: New evidence of warming propagating toward the Arctic Ocean, Geophys. Res. Lett., 33, https://doi.org/10.1029/2006GL025872, 2006.
- Wawrzyniak, T. and Osuch, M.: A 40-year High Arctic climatological dataset of the Polish Polar Station Hornsund (SW Spitsbergen, Svalbard), Earth Syst. Sci. Data, 12, 805–815, https://doi.org/10.5194/essd-12-805-2020, 2020.

- Weber, T. C. and Ward, L. G.: Observations of backscatter from sand and gravel seafloors between 170 and 250 kHz, The Journal of the Acoustical Society of America, 138, 2169–2180, https://doi.org/10.1121/1.4930185, 2015.
- Weidner, E.: Angular dependence of backscattering between 170 and 250 kHz from the terminus of a tidewater glacier, The Journal of the Acoustical Society of America, 158, 504–514, https://doi.org/10.1121/10.0037196, 2025.
- Weidner, E. F. and Deane, G.: Hornsund Fjord 2023: Broadband Active Acoustic and Oceanographic Data, UC San Diego Library Digital Collections [data set], https://doi.org/10.6075/J0N87B1B, 2024.
- Weidner, E. and Weber, T. C.: Broadband acoustic characterization of backscattering from a rough stratification interface, The Journal of the Acoustical Society of America, 155, 114–127, https://doi.org/10.1121/10.0024148, 2024.
- Weidner, E., Weber, T. C., Mayer, L., Jakobsson, M., Chernykh, D., and Semiletov, I.: A wideband acoustic method for direct assessment of bubble-mediated methane flux, Cont. Shelf Res., 173, 104–115, https://doi.org/10.1016/j.csr.2018.12.005, 2019.
- Weidner, E., Stranne, C., Sundberg, J. H., Weber, T. C., Mayer, L., and Jakobsson, M.: Tracking the spatiotemporal variability of the oxic–anoxic interface in the Baltic Sea with broadband acoustics, ICES Journal of Marine Science, 77, 2814–2824, https://doi.org/10.1093/icesjms/fsaa153, 2020.
- Xu, G., Jackson, D. R., and Bemis, K. G.: The relative effect of particles and turbulence on acoustic scattering from deep sea hydrothermal vent plumes revisited, The Journal of the Acoustical Society of America, 141, 1446–1458, https://doi.org/10.1121/1.4974828, 2017.
- Xu, Y., Rignot, E., Menemenlis, D., and Koppes, M.: Numerical experiments on subaqueous melting of Greenland tidewater glaciers in response to ocean warming and enhanced subglacial discharge, Ann. Glaciol., 53, 229–234, https://doi.org/10.3189/2012AoG60A139, 2012.
- Xu, Y., Rignot, E., Fenty, I., Menemenlis, D., and Flexas, M. M.: Subaqueous melting of Store Glacier, west Greenland from three-dimensional, high-resolution numerical modeling and ocean observations, Geophys. Res. Lett., 40, 4648–4653, https://doi.org/10.1002/grl.50825, 2013.
- Young, R. A., Merrill, J. T., Clarke, T. L., and Proni, J. R.: Acoustic profiling of suspended sediments in the marine bottom boundary layer, Geophys. Res. Lett., 9, 175–178, https://doi.org/10.1029/GL009i003p00175, 1982.